
Hoek & Brown model with softening

ADVANCED SOIL MODELS



Last Updated: December 09, 2019

Table of Contents

Chapter 1: Introduction	3
General concepts	5
Mathematical Notation	6
Chapter 2: Model Formulation	8
A Hoek & Brown model with Softening (HBS)	8
Softening Rules	9
Strength Softening Model (SSM)	10
GSI Softening Model (GSM)	10
A cut-off function for the tensile behaviour	13
A non-linear dilation model for rock masses	14
A dilation model within a HB framework	14
Derivation of the parameter $m\psi_0$	15
Chapter 3: UDSM implementation in PLAXIS finite element code	17
Chapter 4: Model Performance	20
Parametric studies	20
Model Calibration	25
Chapter 5: Modeling Strain Localization	28
Viscous regularization technique	28
Strain localization analysis	29
Chapter 6: Simulation of Tunnel Excavation	34
Case study: Donking-Morien Tunnel	37
Chapter 7: References	38
Appendix A: Appendix	41

Hoek & Brown (HB) failure criterion has been often employed over the past decades in practical engineering applications due to its intrinsic capability to capture the non-linear behavior of different types of rocks. The former idea of HB ([Hoek, 1968](#) (on page 39); [Hoek and Brown, 1980](#) (on page 39)), was to link some concepts of fracture mechanics and the macroscopic response resulting from the non-linear trend of the initial yielding. To formulate a mathematical expression of the initial yield surface and describe the rock-mass behavior, the Uniaxial Compression Strength (*UCS*) of the intact rock and some dimensionless constants obtained from empirical correlations (i.e., the constants m_b , s and a) have been used to define the HB criterion:

$$\sigma_1 = \sigma_3 + [m_b(\sigma_3 / \sigma_{ci}) + s]^a \quad \text{Eq. [1]}$$

where

σ_1	=	Major principal effective stress.
σ_3	=	Minor principal effective stress.
σ_{ci}	=	<i>UCS</i> of the intact material.
a, m_b, s	=	Dimensionless coefficient prescribing the non-linear trend of the initial yield surface obtained from empirical correlations.

This approach has been further improved by several authors ([Marinos et al., 2005](#) (on page 39)) who have used empirical data recorded from field observations at different environmental conditions to characterize the mechanical properties of the rock-mass. For this purpose, the Geological Strength Index (*GSI*) and the Damage factor (*D*) have been used to define the material parameters of the HB yield surface:

$$\begin{cases} m_b = m_i \exp\left(\frac{GSI - 100}{28 - 14D}\right), \\ s = \exp\left(\frac{GSI - 100}{9 - 3D}\right), \\ a = \frac{1}{2} + \frac{1}{6} \left[\exp\left(-\frac{GSI}{15}\right) - \exp\left(-\frac{20}{3}\right) \right] \end{cases} \quad \text{Eq. [2]}$$

In these equations, m_i is the value of m_b corresponding to the intact rock (i.e., $m_b \equiv m_i$ for $GSI=100$). Hereafter, the Hoek & Brown model implemented in PLAXIS refers to the formulation proposed by [Jiang \(2017\)](#) (on page 39) which can guarantee at the same time smoothness and convexity of the yield surface and plastic potential. The underlying implementation is further enhanced with the following constitutive features:

- The initial non-associativity with the ability to simulate the non-linear evolution of the dilation in the post-peak regime.
- A softening rule implemented through two different formulations.
- A tension cut-off in the tensile regime of the stress space.
- A rate-dependent version of the HB model is here used to solve the mesh-dependency of the numerical solution when the brittle failure is characterized by a strong concentration of strain in narrow shear bands.

Introduction

A sketch of the material response is illustrated in *Figure 1* and *Figure 2* where the corresponding mechanical material behavior is depicted in combination with the interplay of the softening mechanisms governing the post-peak regime.

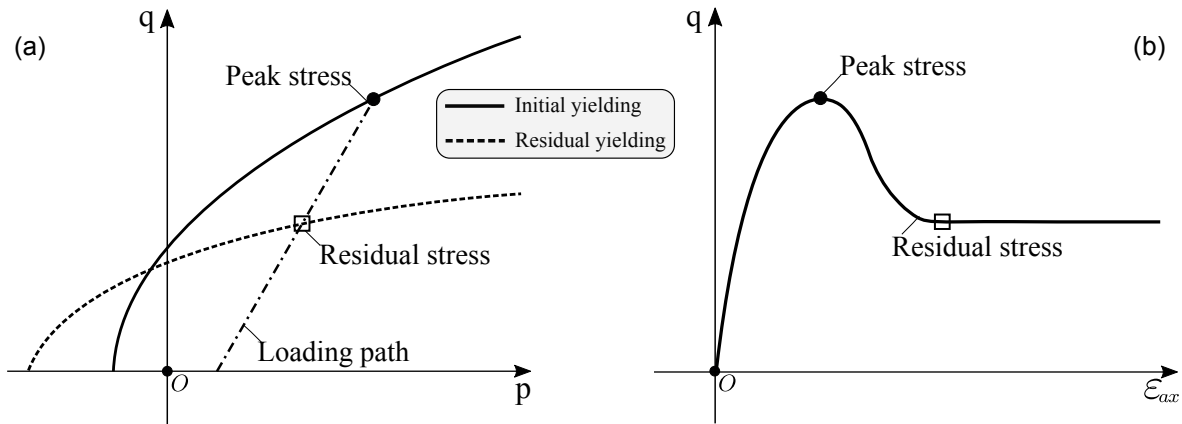


Figure 1: Material behavior under triaxial stress path: (a) Initial and residual yield surfaces during the stress path, (b) The peak and residual strength in the stress-strain space.

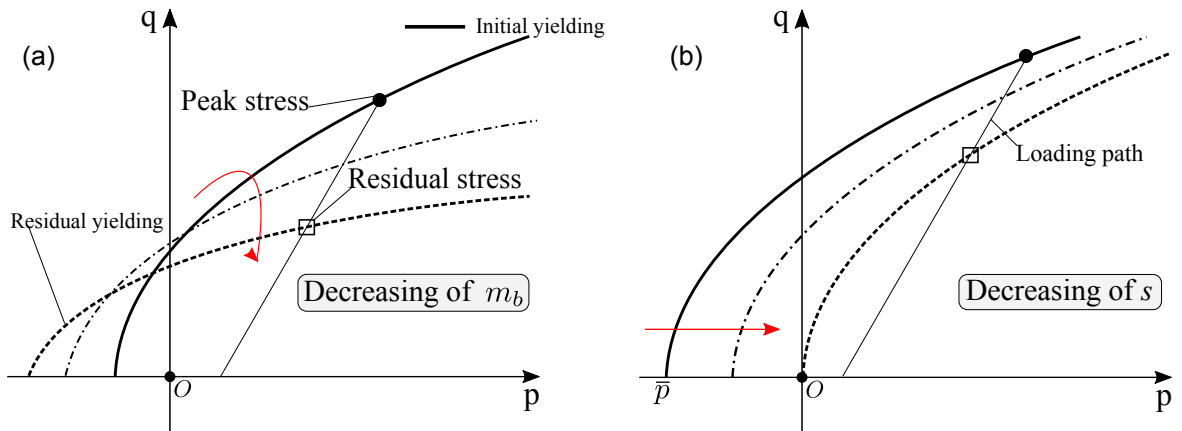


Figure 2: Effects of the Softening process on the variables (a) m_b and (b) s on the yield surface.

In the following sections, after presenting the mathematical formulation of the constitutive equations ([Model Formulation](#) (on page 8)) with particular focus on the material parameters used in the modeling ([UDSM implementation in PLAXIS finite element code](#) (on page 17)) some numerical analyses are computed to study the model performance at the Gauss point level ([Model Performance](#) (on page 20)), thus highlighting the effect of some parameters during the material degradation process and the ability of the model in simulating laboratory experiments. The performance of the viscous regularization method to restore the mesh-objectivity during the post-peak regime is illustrated in [Modeling Strain Localization](#) (on page 28) and then employed in [Simulation of Tunnel Excavation](#) (on page 34) to simulate a tunnel excavation problem.

Introduction

General concepts

General concepts

Before detailing the proposed implementation of the Hoek & Brown model, some general concepts related to the elasto-plastic theory are recalled hereafter:

- The strain is additively split in the elastic and plastic components, respectively:

$$\varepsilon_{ij}^t = \varepsilon_{ij}^{el} + \varepsilon_{ij}^{pl}$$

- The stress σ_{ij} is computed with isotropic linear elasticity: $\sigma_{ij} = C_{ijkl} \varepsilon_{kl}^{el}$.
- The yield surface f is used to define the elastic domain and admissibility of the stress state.
- The plastic flow of the model is prescribed through a flow rule:

$$\dot{\varepsilon}_{ij}^{pl} = \dot{\Lambda} \left(\frac{\partial g}{\partial \sigma_{ij}} \right) \quad Eq. [3]$$

where

$$\begin{aligned} g &= \text{Plastic potential function and prescribes the direction of the plastic flow.} \\ \Lambda &= \text{Plastic multiplier for the calculation of the amount of plastic strains.} \end{aligned}$$

- A similar equation is also defined to govern the evolution of the softening variable Γ_i of the model: $\Gamma_i = \dot{\Lambda} h_i$, where h_i is the softening vector of the model.
- The state of the material is governed by the so-called *Khun-Tucker conditions*:

$$f(\sigma_{ij}, \Gamma_k) \leq 0, \quad \dot{\Lambda} f(\sigma_{ij}, \Gamma_k) = 0, \quad \dot{\Lambda} \geq 0 \quad Eq. [4]$$

if $f < 0$ then the material state is elastic (i.e., $\dot{\Lambda} = 0$), while if $f = 0$ the state of the material can be potentially plastic loading (i.e., $\dot{\Lambda} > 0$). To determine if the material state is in plastic loading the same logic can be used by considering further conditions, the so-called persistency conditions:

$$\dot{f}(\sigma_{ij}, \Gamma_k) \leq 0, \quad \dot{\Lambda} \dot{f}(\sigma_{ij}, \Gamma_k) = 0, \quad \dot{\Lambda} \geq 0 \quad Eq. [5]$$

where

$$\begin{aligned} \dot{f} < 0 &= \text{Elastic unloading.} \\ \dot{f} = 0, \dot{\Lambda} > 0 &= \text{Plastic loading.} \\ \dot{f} = 0, \dot{\Lambda} = 0 &= \text{Neutral loading.} \end{aligned}$$

The proposed implementation allows users to adopt the model also within a visco-plastic framework. Specifically, reference will be made to the over-stress theory formulated by [Perzyna \(1966\)](#) (on page 39) in which the stress is not constrained to lay on the yield surface as in the elasto-plastic theory. In this framework, the increment of visco-plastic strain is computed as:

$$\dot{\varepsilon}_{ij}^{vp} = \Phi(f) \left(\frac{\partial g}{\partial \sigma_{ij}} \right) \quad Eq. [6]$$

where

$$\Phi(f) = \text{Viscous nucleus function, which represents a measure of the distance between the current stress state and the yield surface.}$$

Introduction

General concepts

Mathematical Notation

It is common practice in geomechanical modeling to express the stress dependency of the yield and plastic potential surfaces as a function of stress invariants, i.e., the mean stress p , the stress deviator q and the Lode's angle θ . They are defined as:

$$\begin{cases} p = \frac{tr(\sigma)}{3} = \frac{\sigma_{ij} \cdot \delta_{ij}}{3} = \frac{\sigma_{xx} + \sigma_{yy} + \sigma_{zz}}{3} \\ q = \sqrt{\frac{3}{2}}(s_{ij}s_{ij}) = \sqrt{\frac{3}{2}}\|s\| \\ \theta = \frac{1}{3} \arcsin \left[\sqrt{6} \left(\frac{tr(s^3)}{tr(s^2)^{3/2}} \right) \right] \end{cases}$$

where

$$\begin{aligned} s_{ij} &= \text{Deviator component of the stress state (i.e., } s_{ij} = \sigma_{ij} - p \cdot \delta_{ij} \rightarrow \delta_{ij} \text{ is Kronecker's symbol)} \\ tr(\cdot) &= \text{Trace that gives the sum of the diagonal terms of the matrix (i.e., } tr(\sigma_{ij}) = \sigma_{xx} + \sigma_{yy} + \sigma_{zz} = 3P). \end{aligned}$$

A general representation of the stress deviator and its norm is reported as:

$$s_{ij} = \begin{bmatrix} \sigma_{xx} - p & \sigma_{xy} & \sigma_{xz} \\ \sigma_{yx} & \sigma_{yy} - p & \sigma_{yz} \\ \sigma_{zx} & \sigma_{zy} & \sigma_{zz} - p \end{bmatrix}$$

$$\|s\| = (\sigma_{xx} - p)^2 + (\sigma_{yy} - p)^2 + (\sigma_{zz} - p)^2 + 2(\sigma_{xy}^2 + \sigma_{zy}^2 + \sigma_{zx}^2)$$

Analogously, similar quantities are defined also for the strain tensor ε_{ij} :

$$\begin{cases} \varepsilon_v = \varepsilon_{xx} + \varepsilon_{yy} + \varepsilon_{zz} \\ \varepsilon_q = \sqrt{\frac{2}{3}}(\varepsilon_{s_{ij}} \varepsilon_{s_{ij}}) = \sqrt{\frac{2}{3}}\|\varepsilon_s\| \end{cases}$$

where

$$\begin{aligned} \varepsilon_v &= \text{Volumetric strain.} \\ \varepsilon_{s_{ij}} &= \text{strain deviator. Defined as: } \varepsilon_{s_{ij}} = \varepsilon_{ij} - (\varepsilon_v \cdot \delta_{ij}) / 3 . \end{aligned}$$

$$\varepsilon_{s_{ij}} = \begin{bmatrix} \varepsilon_{xx} - \varepsilon_v / 3 & \varepsilon_{xy} & \varepsilon_{xz} \\ \varepsilon_{yx} & \varepsilon_{yy} - \varepsilon_v / 3 & \varepsilon_{yz} \\ \varepsilon_{zx} & \varepsilon_{zy} & \varepsilon_{zz} - \varepsilon_v / 3 \end{bmatrix}$$

$$\|\varepsilon_s\| = \left(\varepsilon_{xx} - \frac{\varepsilon_v}{3} \right)^2 + \left(\varepsilon_{yy} - \frac{\varepsilon_v}{3} \right)^2 + \left(\varepsilon_{zz} - \frac{\varepsilon_v}{3} \right)^2 + 2(\varepsilon_{xy}^2 + \varepsilon_{zy}^2 + \varepsilon_{zx}^2)$$

For triaxial stress paths ($\sigma_{xx} = \sigma_{yy} < \sigma_{zz}$, $\sigma_{xz} = \sigma_{xy} = \sigma_{yz} = 0$), the general definition of invariants can be simplified as:

Introduction

General concepts

$$p = (\sigma_{zz} + 2\sigma_{xx})/3 \quad q = |\sigma_{zz} - \sigma_{xx}|$$
$$\varepsilon_v = (\varepsilon_{zz} + 2\varepsilon_{xx})/3 \quad \varepsilon_q = 2|\varepsilon_{zz} - \varepsilon_{xx}|/3$$

In this context, the deviatoric and volumetric plastic strain are computed as:

$$\dot{\varepsilon}_v^p = \dot{\lambda} \left(\frac{\partial g}{\partial p} \right); \quad \dot{\varepsilon}_q^p = \dot{\lambda} \left(\frac{\partial g}{\partial q} \right)$$

Hereafter, a positive compression convention will be adopted by following the usual soil mechanics framework.

A Hoek & Brown model with Softening (HBS)

To consider the effect of the intermediate principal stress in the yield surface the generalization of the classical HB in terms of stress invariants (i.e., the mean stress p , the deviator stress q and the Lode's angle θ) has been considered according to mathematical formalism reported in [Jiang and Zhao \(2015\)](#) (on page 39):

$$f = \left(\frac{q}{\sigma_{ci}^{1/\alpha}} \right)^{1/\alpha} + A(\theta) \left(\frac{q}{3} m_b \right) - m_b p - s \sigma_{ci} \quad \text{Eq. [7]}$$

The function $A(\theta)$ considered in the following formulation corresponds to the expression proposed by [Jiang \(2017\)](#) (on page 39) which is defined as:

$$A(\theta) = \frac{\cos \left[\frac{1}{3} \arccos(\kappa \cos 3\theta) \right]}{\cos \left[\frac{1}{3} \arccos(\kappa) \right]} \quad \text{with } -1 < \kappa \leq 0 \quad \text{Eq. [8]}$$

The parameter κ can be considered as a further parameter of the model enabling a better calibration of the rock sample behavior in the deviatoric plane (i.e., $\kappa=0$ corresponds to a circular section while $\kappa \rightarrow -1$ corresponds to the section defined by [Jiang and Zhao \(2015\)](#) (on page 39)). Although the parameter $\kappa \rightarrow -1$ can guarantee a closer approximation of the original HB surface (i.e., Eq. 1), this surface is characterised by a discontinuity of its first derivate (i.e., the gradient of yield surface $\partial f / \partial \sigma_{ij}$) along compressive triaxial stress paths. Therefore, it is recommended to avoid this particular value of κ when computing general three-dimensional IBVPs (Initial Boundary Value Problems) or during triaxial stress path. By default, this parameter is fixed to $\kappa = -0.9999$ if the selected value is out of the range $-1 < \kappa \leq 0$. A representation of the HB criterion proposed by [Jiang \(2017\)](#) (on page 39) is plotted in the deviatoric plane (*Figure 3(a)*) where the yield surface corresponding to the specific value of $\kappa = -0.9$ has been compared to the original HB formulation and a Drucker-Prager surface. By observing this figure, it is worth noting that for axisymmetric stress paths, the 3D generalization proposed by [Jiang \(2017\)](#) (on page 39) (i.e., Eq. 7) converges to the original formulation of the model reported in Eq. 1. In *Figure 3(b)*, the function $A(\theta)$ is also plotted for several value of the parameter κ .

To calculate the plastic strain, the plastic potential has been defined by using the same mathematical characteristics of the yield surface in which they differ only on the basis of the variable m_{ψ} , thus enabling to recover the associated plasticity in case $m_{\psi} \equiv m_b$.

$$g = \frac{q}{\sigma_{ci}^{1/\alpha}} + A(\theta) \frac{q}{3} m_{\psi} - m_{\psi} p, \quad \begin{cases} \dot{\epsilon}_v^p = \dot{\Lambda}(-m_{\psi}) \\ \dot{\epsilon}_q^p = \dot{\Lambda} \left[\frac{1}{\alpha} \left(\frac{q}{\sigma_{ci}} \right)^{1/\alpha-1} + \frac{m_{\psi}}{3} \right] \end{cases} \quad \text{Eq. [9]}$$

Model Formulation

Softening Rules

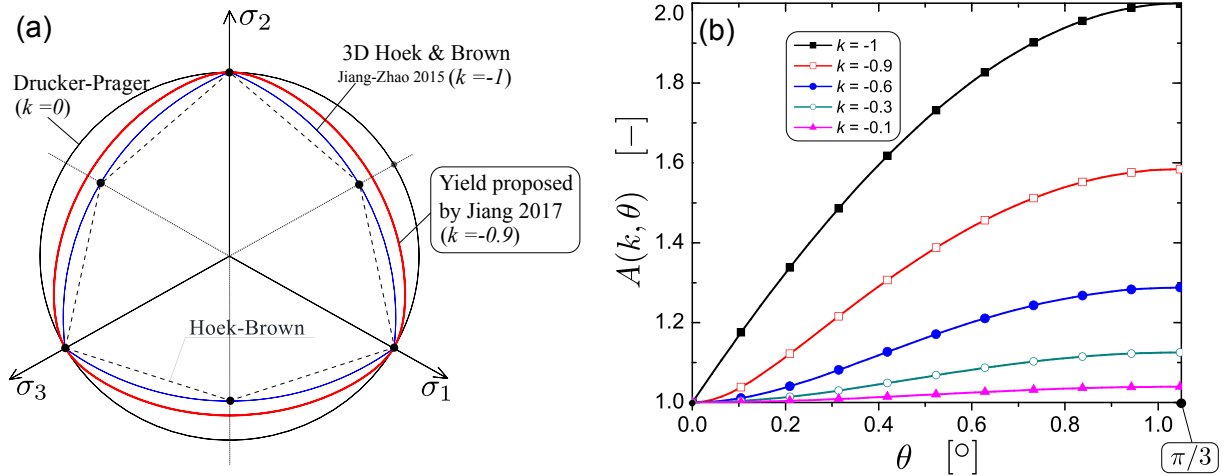


Figure 3: (a) Section of the yield criterion proposed by Jiang (2017) in the deviatoric plane, (b) Evolution of the function $A(\theta, \kappa)$ (figures rearranged after Jiang, 2017)

An overview of the material properties characterizing the HB formulation (i.e., σ_{ci} , m_i) for different types of rocks is reported in the [Appendix](#) (on page 41). This includes also a representation of the *GSI* system, as well as a range of values of the disturbance factor D characterizing several engineering problems.

Softening Rules

The material degradation due to shearing is simulated by means of a softening rule in which a reduction of the hardening variables Γ_j is prescribed as a function of the equivalent plastic strain ε_{eq}^p (i.e., a cumulated value of deviatoric plastic strain), thus enabling to describe the material destructuration due to shearing. Specifically, a hyperbolic decay of Γ_j has been enforced to approach its residual value for large values of plastic strain accordingly with the softening rule proposed by [Barnichon \(1988\)](#) (on page 38) and [Collin \(2003\)](#) (on page 38).

$$\Gamma_j = \Gamma_{j_o} - \left(\frac{\Gamma_{j_o} - \Gamma_{j_r}}{B_j + \varepsilon_{eq}^p} \right) \varepsilon_{eq}^p, \quad \varepsilon_{eq}^p = \int_0^t \dot{\varepsilon}_q^p dt \quad \text{Eq. [10]}$$

where

- o, r = Subscripts indicating the initial and the residual values of Γ .
- B_j = Material parameter governing the rate of softening of the corresponding j -th hardening variable.

Figure 4 shows the normalized change of Γ_j for different values of the parameters B_j , where $B_j = \varepsilon_{eq}^p$ represents the specific value for which Γ_j reaches the 50% degradation (i.e., $\Gamma_j = 0.5 \cdot (\Gamma_{j_o} + \Gamma_{j_r})$).

Two different approaches are considered to implement the softening rule reported in Eq. 10:

1. By defining the decrease of the material properties m_b and s ([Alonso et al., 2003](#) (on page 38); [Zou et al., 2016](#) (on page 40)), hereinafter referred to as *Strength Softening Model (SSM)*,
2. By defining the decrease of the *GSI* index following the suggestion of [Cai et al. \(2007\)](#) (on page 38) (see also [Ranjbarnia et al., 2015](#) (on page 39); [Manouchehrian and Cai, 2017](#) (on page 39)), hereinafter referred to as *GSI Softening Model (GSM)*.

Model Formulation

Softening Rules

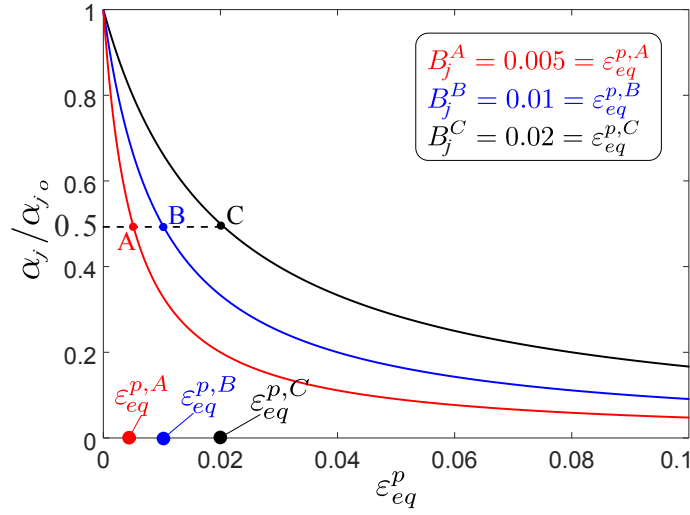


Figure 4: Evolution of the softening variable Γ_j normalized by its initial value. The curves correspond to different values of B_j (i.e., B_j^A , B_j^B and B_j^C) to show the influence of the parameter B_j on the rate of softening.

Strength Softening Model (SSM)

In this approach the decrease of the material properties is applied explicitly to the variables m_b and s as implemented in [Marinelli et al. \(2019\)](#) (on page 39), thus enabling to rearrange Eq. 10 as:

$$\Gamma = \begin{bmatrix} m_b \\ s \end{bmatrix} = \begin{bmatrix} m_{b_0} - \left(\frac{m_{b_0} - m_{b_r}}{B_m + \varepsilon_{eq}^p} \right) \varepsilon_{eq}^p \\ s_0 - \left(\frac{s_0 - s_r}{B_s + \varepsilon_{eq}^p} \right) \varepsilon_{eq}^p \end{bmatrix} \quad \text{Eq. [11]}$$

GSI Softening Model (GSM)

A different strategy to enforce the material degradation consists to use the *GSI* index as a hardening variable of the model, thus applying the decrease of the material softening through the empirical relations reported in Eq. 2. This strategy is consistent with the investigation proposed by [Cai et al. \(2004, 2007\)](#) (on page 38) to determine the residual properties of the rock mass in which the softening process is associated with a combination of two main factors:

1. The development of micro-cracks, fractures and discontinuities.
2. The smoothing of the joint surface, affecting the joint strength (see [Figure 5](#)).

According to this approach, the degradation of the rock quality is reflected through a decrease of the *GSI*:

$$GSI = GSI_o - \left(\frac{GSI_o - GSI_r}{B_{GSI} + \varepsilon_{eq}^p} \right) \varepsilon_{eq}^p \quad \text{Eq. [12]}$$

where

$$\begin{aligned} GSI_o, GSI_r &= \text{Initial and the residual values of } GSI. \\ B_{GSI} &= \text{Parameter controlling the rate of softening.} \end{aligned}$$

Model Formulation

Softening Rules

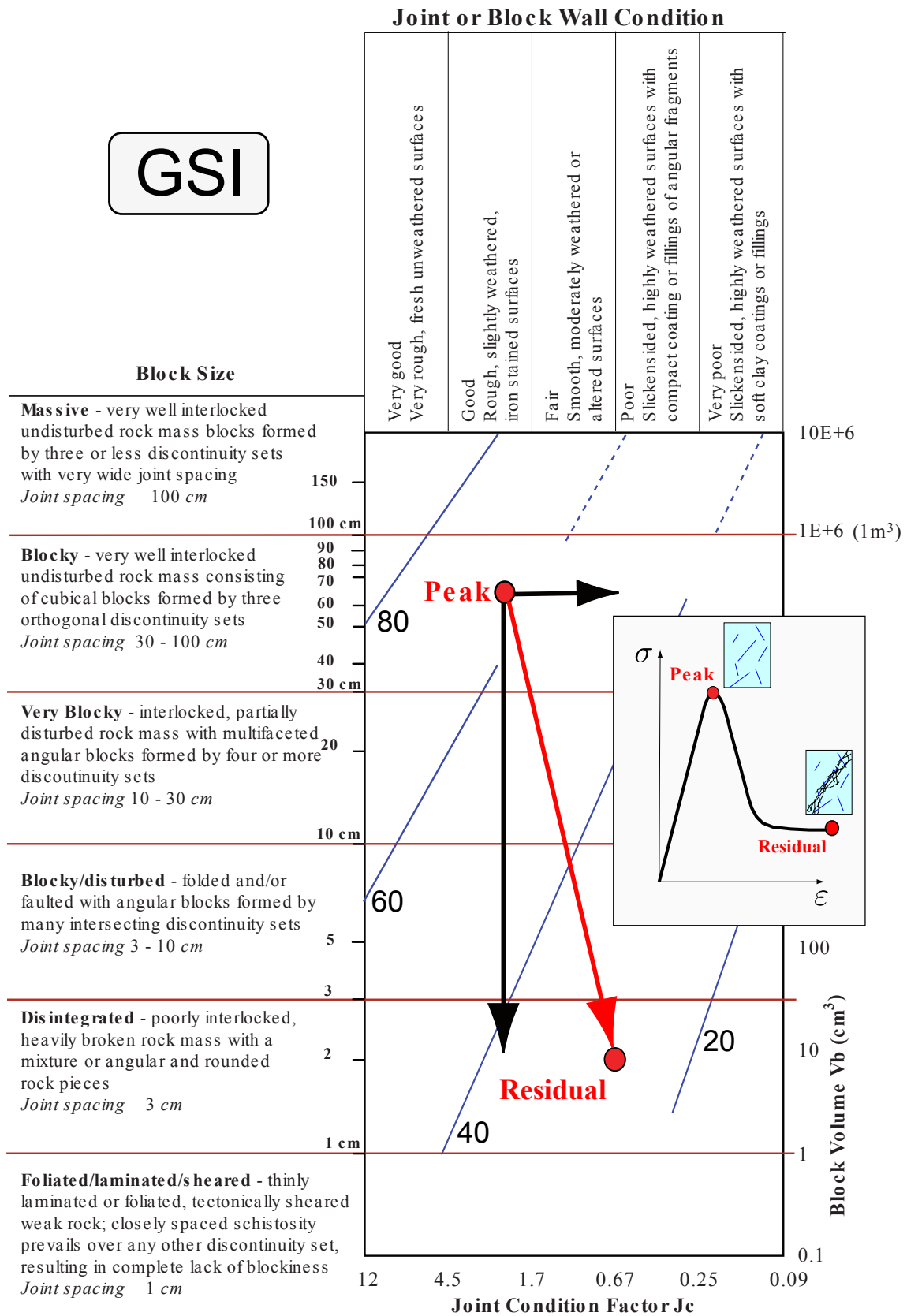


Figure 5: Evolution of GSI during the degradation process of the rock mass (figure after Cai et. al [2017])

Model Formulation

Softening Rules

By replacing Eq. 12 in Eq. 2, it is possible to obtain a generalized expression of the softening rule for the *GSM* approach:

$$\Gamma = \begin{bmatrix} m_b \\ s \end{bmatrix} = \begin{pmatrix} m_{b_o} \exp \left[\left(\frac{GSI_r - GSI_o}{28 - 14D} \right) \left(\frac{\varepsilon_{eq}^p}{B_{GSI} + \varepsilon_{eq}^p} \right) \right] \\ s_o \exp \left[\left(\frac{GSI_r - GSI_o}{9 - 3D} \right) \left(\frac{\varepsilon_{eq}^p}{B_{GSI} + \varepsilon_{eq}^p} \right) \right] \end{pmatrix} \quad Eq. [13]$$

It is important to remark that, to be consistent with the definition of the parameters defining the yield criterion and the *GSI* system (see Eq. 2), the exponent a might be added between the hardening variables reported in the vector Γ , thus having a further dependency between a and *GSI*. For the sake of simplicity, and also due to the limited range of variability of a , this coefficient will be kept constant and, accordingly, will be defined by using the initial *GSI* value (i.e., $a = 0.5 + [\exp(-GSI_o / 15) - \exp(-20 / 3)] / 6$).

In the last decades, to evaluate the residual values of m_b and s , several empirical relations have been proposed in literature. [Ribacchi \(2000\)](#) (on page 39) proposed to compute m_b and s_r as a fraction of their initial values (i.e., $m_b = 0.65m_{b_o}$ and $s_r = 0.04s_o$), while [Crowder and Bawden \(2004\)](#) (on page 39) improved this logic by suggesting different residual values in relation to different values of the *GSI*. Along these lines, [Cai et al. \(2007\)](#) (on page 38) and [Alejano et al. \(2010\)](#) (on page 38) have proposed the following empirical relation of GSI_r as a function of GSI_o :

$$\begin{aligned} GSI_r &= GSI_o e^{-0.0134GSI_o}, & 25 < GSI_o < 75 & \text{Cai et al. (2007)} \\ GSI_r &= 17.34e^{0.0107GSI_o}, & 25 < GSI_o < 75 & \text{Alejano et al. (2010)} \end{aligned} \quad Eq. [14]$$

The evolution of GSI_r according to Eq. 14 is plotted in *Figure 6* where the quality of the rock is reported in relation to the initial value of GSI_o . By observing this figure, it is worth remarking that, for values of GSI_o smaller than $GSI_o = 25$ it is suggested to consider a cut-off of Eq. 14 as shown in *Figure 6*, due to the lack of variability of the parameters m_b , s_o and a calculated with $GSI_o \leq 25$.

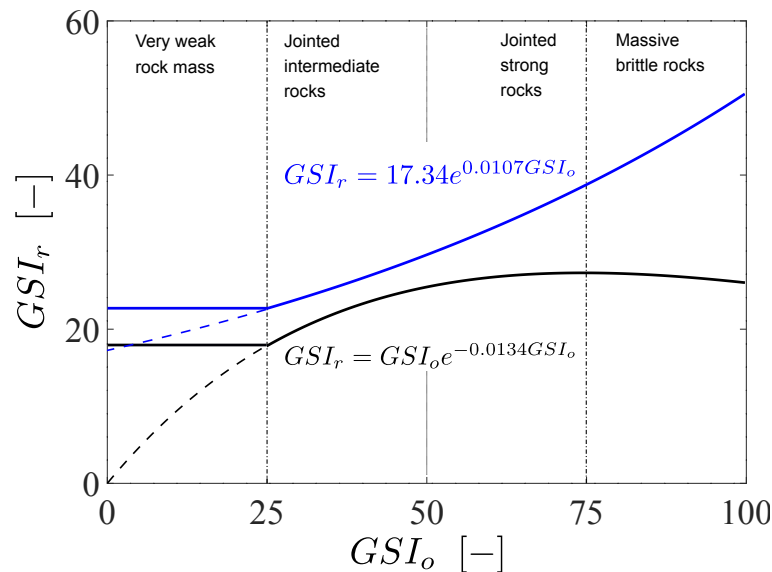


Figure 6: Evolution of GSI_r according to [Cai et al. \(2007\)](#) and [Alejano et al. \(2010\)](#).

Model Formulation

A cut-off function for the tensile behaviour

A cut-off function for the tensile behaviour

In order to introduce a cut-off function in the tensile regime, the value of the mean stress \bar{p} at the corner of the HB surface (i.e., $\bar{p} = s_o \sigma_{ci} / m_{b_o}$) is reduced through the parameter α which ranges of values between 0 to 1 (Figure 7), thus defining the mean stress p^* limiting the maximum tensile stress of the model:

$$0 \leq \alpha \leq 1 \quad \begin{cases} \alpha = 1 : \text{no cut-off function} \rightarrow p^* = \bar{p} \\ \alpha = 0 : \text{no tensile domain} \rightarrow p^* = 0 \end{cases} \quad \text{Eq. [15]}$$

An associated plastic flow is considered in the tensile zone of the stress-space (i.e., $f \equiv g$) which is characterized by a perfect plastic mechanism (i.e., $m_b \equiv m_{b_o}$ and $s \equiv s_o$). The user can estimate the value of α and the corresponding value of p^* starting from the tensile strength σ_t obtained from laboratory tests. For this purpose, if the tensile strength σ_t is available from a uniaxial tension test, the mean stress p^* at which the material fails due to tensile strength is equal to $p^* = \sigma_t / 3$. As a result, the value of α corresponding to the specific tensile strength σ_t is calculated as:

$$p^* = \alpha \bar{p} = \frac{\sigma_t}{3} = \alpha \left(\frac{\sigma_{ci}}{\sigma_t} \right), \quad \alpha = \frac{1}{3} \left(\frac{\sigma_t}{\sigma_{ci}} \right) \frac{m_{b_o}}{s_o} \quad \text{Eq. [16]}$$

For intact rock, Eq. 16 is rewritten as $\alpha = (\sigma_t / \sigma_{ci}) \cdot (m_i / 3)$.

By default, a value of $\alpha=0.5$ is suggested.

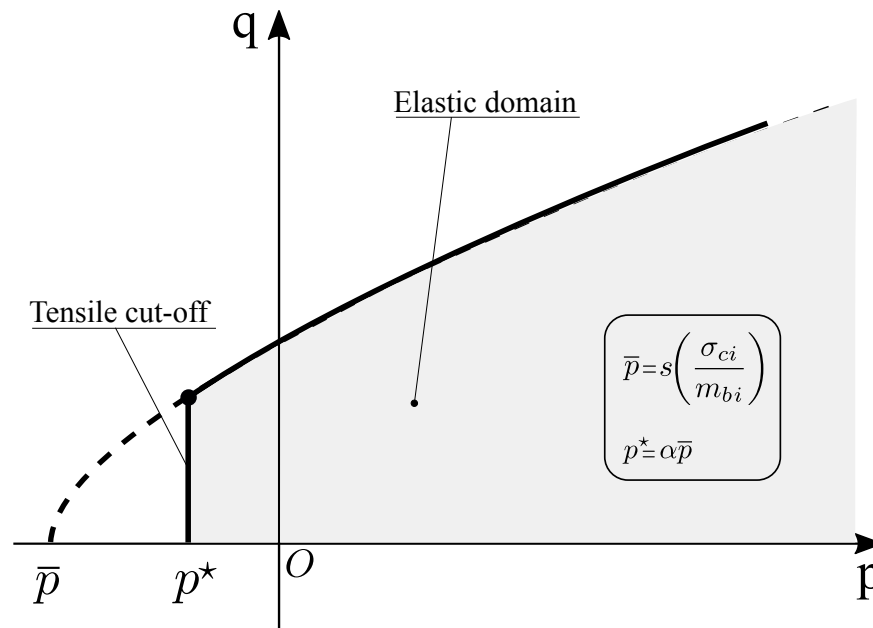


Figure 7: Sketch of the cut-off function in the tensile regime

Model Formulation

A non-linear dilation model for rock masses

A non-linear dilation model for rock masses

Understanding the post-yielding behavior of a rock mass and the evolution of strains are critical ingredients for geostucture design. For tunneling problems, an accurate prediction of the strain field and the corresponding plastic radius have a strong influence on support and reinforcement design. As a result, a detailed modeling of the evolution of volumetric strain during the post-peak regime is required. For this purpose, it is common practice to introduce the dilation angle ψ defined as ([Vermeer and De Borst, 1984](#) (on page 39)):

$$\sin \psi = \frac{\dot{\varepsilon}_v^p}{-2\dot{\varepsilon}_1^p + \dot{\varepsilon}_v^p}, \quad \text{or equivalently,} \quad \dot{\varepsilon}_v^p = 2\dot{\varepsilon}_1^p \left(\frac{\sin \psi}{\sin \psi - 1} \right) \quad \text{Eq. [17]}$$

By substituting the plastic potential (i.e., Eq. 9) in Eq. 17, it is possible to relate the dilation angle with the parameters of a HB model:

$$\sin \psi = \frac{m_\psi}{\frac{2}{a} \left(\frac{q}{\sigma_{ci}} \right)^{1/a-1} + m_\psi} \quad \text{Eq. [18]}$$

Under triaxial conditions Eq. 18 is equivalent to the classical formulation reported in Eq. 1, which can be used to rearrange the dilatancy as:

$$\sin \psi = \frac{m_\psi}{\frac{2}{a} \left(m_b \frac{\sigma_3}{\sigma_{ci}} + s \right)^{1-a} + m_\psi} \quad \text{Eq. [19]}$$

or equivalently:

$$m_\psi = \frac{2}{a} \left[\frac{\sin \psi}{1 - \sin \psi} \right] \left(m_b \frac{\sigma_3}{\sigma_{ci}} + s \right)^{1-a} \quad \text{Eq. [20]}$$

In Eq. 20, the non-linear variability of m_ψ can be prescribed by using explicitly one of the formulations proposed in literature for the dilation angle to define the evolution of m_ψ as a function of plastic strain ([Alejano and Alonso, 2005](#) (on page 38); [Zhao and Cai, 2010](#) (on page 40); [Walton and Diederichs, 2015](#) (on page 40); [Rahjoo et al., 2016](#) (on page 39)). In the proposed model the trend of behaviour of the dilation angle is enforced through an explicit variability of m_ψ for both the *SSM* and *GSM* formulations, thus guaranteeing a smooth transition between associated and a non-associated plasticity, as well as the reduction of the dilatancy angle along the degradation process. Although Eq. 20 is not considered for the modeling of the dilatant behaviour of the rock, this equation will be taken into account to determine the initial values of the parameter m_{ψ_0} .

A dilation model within a HB framework

The evolution of the variable m_ψ for the two approaches is expressed as:

$$m_\psi = m_{\psi_0} - \left(\frac{m_{\psi_0} - m_{\psi_r}}{B_\psi + \varepsilon_{eq}^p} \right) \varepsilon_{eq}^p, \quad \text{SSM approach} \quad \text{Eq. [21]}$$

This equation can be further rearranged by assuming a vanishing value of m_{ψ_r} (i.e., $m_{\psi_r} \approx 0$) which enables the following simplification:

Model Formulation

A non-linear dilation model for rock masses

$$m_{\psi} = \left(\frac{B_{\psi}}{B_{\psi} + \varepsilon_{eq}^p} \right) m_{\psi_0} \quad Eq. [22]$$

Along these lines, a similar dependency employed to define the evolution of m_b and GSI , is proposed to formulate the variable m_{ψ} in the GSM approach:

$$m_{\psi} = m_{\psi_0} \left[\frac{GSI - 100}{F_{\psi}(28 - 14D)} \right]; \quad \underline{GSM\ approach} \quad Eq. [23]$$

where

$$F_{\psi} = \text{Parameter introduced to control the decrease of } m_{\psi} \text{ with the reduction of the } GSI.$$

By substituting Eq. 12 into Eq. 23, it is possible to rewrite m_{ψ} analogously to Eq. 13:

$$m_{\psi} = m_{\psi_0} \exp \left[\left(\frac{GSI_r - GSI_o}{F_{\psi}(28 - 14D)} \right) \left(\frac{\varepsilon_{eq}^p}{B_{GSI + \varepsilon_{eq}^p}} \right) \right] \quad Eq. [24]$$

Furthermore, to separate the effect of the parameter accounting for the quality of the rock mass from the contribution of the intact rock, F_{ψ} is rewritten as:

$$F_{\psi} = \left(\frac{GSI_o^i - GSI_r^i}{GSI_o^i - GSI_r^i} \right) F_{\psi}^i \quad Eq. [25]$$

where

$$\begin{aligned} GSI_o^i, GSI_r^i &= \text{Initial and residual values of } GSI \text{ of the intact rock sample (i.e., } GSI_o^i = 100 \text{ and } GSI_r^i \approx 35). \\ F_{\psi}^i &= \text{Dilation rate of the intact rock, thus enabling its calibration with experimental tests.} \end{aligned}$$

Although the user can determine the value of m_{ψ_0} by calibrating this parameter with results obtained from laboratory tests (as in the calibration proposed by [Marinelli et al., 2019](#) (on page 39)), in the next section a strategy enabling a qualitative evaluation of m_{ψ_0} is presented to link the selected formulation with empirical relations proposed in literature.

Derivation of the parameter m_{ψ_0}

In this section, a possible strategy to introduce the dependency of the GSI on the value of the initial dilation angle is presented. For this purpose, Eq. 20 is considered to characterize the dilation at the initial yielding (i.e., the values of the parameters m_{b_0} and ψ_0):

$$m_{\psi_0} = \frac{2}{a} \left[\frac{\sin(\psi_o^{rm})}{1 - \sin(\psi_o^{rm})} \right] \left(m_{b_0} \frac{\sigma_3}{\sigma_{ci}} + s_o \right)^{1-a} \quad Eq. [26]$$

In this equation, the effect of the rock mass will emerge not only on the parameters of the HB yield criterion (i.e., m_{b_0} and s_o) but also on the expression of the initial dilation angle ψ_o^{rm} (the apex rm stands for *rock mass*). The rock mass effect will be introduced through a scalar quantity ξ consistently with formulation proposed by [Alejano et al. \(2010\)](#) (on page 38) (i.e., $\psi_o^{rm} \equiv \xi \psi_o^{ir}$ where the apex ir stands for *intact rock*).

Model Formulation

A non-linear dilation model for rock masses

Intact rock

In the proposed model, both the strength degradation and the evolution of the dilatant behaviour of the intact rock neglect the potential dissipative phenomena before the peak. For this reason, the initial dilation angle can be considered coincident with its peak value (i.e., $\psi_o^{ir} \equiv \xi \psi_{peak}^{ir}$) which can be used to calculate m_{ψ_o} (the apex *ir* stands for *intact rock*). Instead of calibrating the parameter m_{ψ_o} with experimental results, it is possible to employ formulations proposed in literature to evaluate the peak dilation angle. Hereafter, the Eq.27 proposed by [Walton and Diederichs \(2015\)](#) (on page 40) is considered:

$$\psi_{peak} = \begin{cases} \varphi_{peak} \left(1 - \frac{\beta'}{\Omega} \sigma_3\right), & \text{if } \sigma_3 < \Omega \\ \varphi_{peak} (\beta_0 - \beta' \ln \sigma_3), & \text{if } \sigma_3 > \Omega \end{cases} \quad \text{with } \Omega = e^{-(1-\beta_0-\beta')/\beta'} \quad \text{Eq. [27]}$$

where

$$\begin{aligned} \beta_0, \beta' &= \text{Parameters that control the pressure sensitivity for high and low confinements respectively (recommended values for crystalline rocks are } \beta_0 = 1 \text{ and } \beta' = 0.1, \text{ } \text{Walton and Diederichs [2015] (on page 40)).} \\ \varphi_{peak} &= \text{Peak friction angle of the material.} \end{aligned}$$

In this equation, it is necessary to calculate also the peak friction angle which can be related to the material properties of the HB model ([Alejano and Alonso, 2005](#) (on page 38)):

$$\sin \varphi_{peak} = \frac{m_b}{\frac{2}{a} \left(m_b \frac{\sigma_3}{\sigma_{ci}} + s \right)^{1-a} + m_b} \quad \text{Eq. [28]}$$

For rock samples, intact rock parameters (i.e., $a=0.5$, $m_b \equiv m_i$) are replaced in Eq. 28, thus obtaining:

$$\sin \varphi_{peak} = \frac{m_i}{4 \sqrt{m_i \left(\frac{\sigma_3}{\sigma_{ci}} \right) + 1} + m_i} \quad \text{Eq. [29]}$$

Effect on the rock mass

To re-scale the value of the peak dilation angle due to the effect of discontinuities characterizing a rock mass, ψ_o^{rm} is calculated on the basis of ψ_o^{ir} and the scalar quantity ξ which is expressed as function of the *GSI* index ([Hoek and Brown, 1997](#) (on page 39); [Alejano and Alonso, 2005](#) (on page 38)). For this reason, a linear trend has been assumed, consistently with the variability of the average dilation angle proposed by [Alejano et al. \(2010\)](#) (on page 38).

$$\psi_o^{rm} = \xi \cdot \psi_{peak}^{ir}, \quad \xi = \begin{cases} 0, & GSI_o \leq 25 \\ (GSI_o - 25) / 50, & 25 \geq GSI_o < 75 \\ 1, & GSI_o \geq 75 \end{cases} \quad \text{Eq. [30]}$$

where

$$\xi = \text{Coefficient accounting for the initial condition of the rock mass and it is defined through the Geological Strength Index (i.e., the value of } GSI_o \text{).}$$

Eq. 30, emphasizes the dilatant characteristics of a rock mass in relation to its mechanical quality. Rock masses characterized by poor quality (i.e., $GSI_o \leq 25$) are associated to a zero-dilatancy, while rock masses in good conditions (i.e., $GSI_o \geq 75$) the value of the dilation angle is the same than the dilation angle of the intact rock.

3

UDSM implementation in PLAXIS finite element code

The HBS has been implemented as a User Defined Soil Model (UDSM) for Plaxis through a DLL format. Both the softening rules have been introduced in the same DLL subroutine and they can be selected as shown in *Figure 8* and *Figure 9*.

User-defined model			
DLL file	hb_soft64.dll		
Model in DLL	HB_SSM		
Parameters			
E	kN/m ²		0.00000
ν			0.00000
D			0.00000
GSI _{ini}	Parameters in common with the GSM softening		0.00000
α			0.00000
m_i			0.00000
$m_{\psi_{ini}}$			0.00000
m_{res}		Parameters specific for the SSM softening	0.00000
s_{res}			0.00000
$m_{\psi_{res}}$			0.00000
σ_{ci}	kN/m ²		0.00000
B_{m_b}			0.00000
B_s			0.00000
B_{ψ}			0.00000
γ	Parameters in common with the GSM softening		0.00000
k			0.00000

Figure 8: Model parameters in PLAXIS for the SSM formulation. The Parameters in common with both softening rules are framed within a black rectangle while the parameters specific for the SSM softening are framed within a red rectangle.

UDSM implementation in PLAXIS finite element code

User-defined model			
DLL file	hb_soft64.dll		
Model in DLL	HB_GSM		
Parameters			
E	kN/m ²		0.00000
ν			0.00000
D	Parameters in common with the SSM softening		0.00000
GSI_{ini}			0.00000
α			0.00000
m_i			0.00000
$m_{\psi_{ini}}$			0.00000
GSI_{res}			0.00000
σ_{ci}	kN/m ²	Parameters specific for the GSM softening	0.00000
B_{gsi}			0.00000
F_{ψ}			0.00000
γ	Parameters in common with the SSM softening		0.00000
k			0.00000

Figure 9: Model parameters in PLAXIS for the GSM formulation. Parameters in common with both softening rules are framed within a black rectangle while the parameters specific for the GSM softening are framed within a red rectangle.

The specific meaning of each parameter is reported below:

- Parameters in common with both softening rules:

E Young modulus.

ν Poisson ratio.

D Disturbance factor.

GSI_{ini} Initial GSI (ie., the variable GSI_0).

α Factor for reducing the tensile strength.

m_i Dimensionless parameter of the intact rock.

$m_{\psi_{ini}}$ Initial value of m_{ψ} (ie., the variable m_{ψ_0}).

σ_{ci} Uniaxial compression strength.

γ Fluidity (inverse of viscosity).

k Parameter governing the shape of the yield surface in the deviatoric plane.

- Parameters for the SSM softening:

$m_{b_{res}}$ Value of the residual quantity of m_b (ie., the variable m_{b_0}).

UDSM implementation in PLAXIS finite element code

s_{res}	Value of the residual quantity of s (i.e., the variable s_r).
$m_{\psi_{res}}$	Value of the residual quantity of m_{ψ} (i.e., the variable $m_{\psi,r}$).
B_{m_b}, B_s	Parameters governing the softening process.
$B_{m_{\psi}}$	Parameter governing the rate of dilation.

- Parameters for the GSM softening:

GSI_{res}	Value of the residual quantity of m_b (i.e., the variable $m_{b,r}$).
B_{GSI}	Parameters governing the softening process.
F_{ψ}	Parameter governing the rate of dilation.

It is worth remarking that, as illustrated in *Figure 3*, the parameter k controls the shape of the deviatoric plane and its range of admissible values varies between zero (circular shape) and minus one (shape of the yield surface according to [Jiang and Zhao, 2015](#) (on page 39)):

$$-1 < k \leq 0 \quad \text{Eq. [31]}$$

If the user select a value of k which is out from this range of admissibility, k will be automatically set equal to -0.9999 .

In both approaches, the last parameter γ represents a fluidity (i.e., the inverse of a viscosity) and will be employed to restore the mesh-objectivity of numerical solutions characterized by localized strains. In this context the parameter γ is also used as flag to allow the user to switch between a pure inviscid/elasto-plastic implementation and its rate-dependent counterpart. In other words, when $\gamma \leq 0$ the model is elasto-plastic, while when $\gamma > 0$ the constitutive equations are visco-plastic with γ defining the fluidity of the model (i.e., the inverse of the viscosity), thus prescribing the rate-sensitivity of mechanical response:

- $\gamma > 0$ Visco-plasticity (rate-dependent response).
- $\gamma \leq 0$ Elasto-plasticity (rate-independent response).

The introduction of visco-plasticity has not only the ability to simulate rate-dependent effect due to fast dynamics process but has also an effect to regularize IBVPs during the development of strain localization. This particular feature will be detailed in [Modeling Strain Localization](#) (on page 28) with particular emphasis on the beneficial effect introduced by the temporal gradient within the visco-plastic theory proposed by the pioneering contribution of [Perzyna \(1966\)](#) (on page 39).

The state variable of the model can be plotted through PLAXIS **output** by selecting **Stresses > State parameters > User > User-defined parameters** . Four state-variables can be plotted:

- ε_p^{eq} (Eq.10)
- m_b and s (Eq. 11 or Eq. 13)
- m_{ψ} (Eq. 21 or Eq. 23)
- The last state variable is not referred to any specific variable but it is just used internally to initialize the problem at the beginning of the computation.

4

Model Performance

Parametric studies

To investigate the performance of the proposed constitutive equations, sensitivity studies have been performed through a set of drained triaxial tests performed at 5 MPa of confining pressure. The set of parameters calibrated in [Marinelli et al. \(2019\)](#) (on page 39) to simulate the Rothbach sandstone has been selected as a reference (see *Table 1*).

Table 1: Model parameters employed to calibrate Rothbach sandstone by using the SSM approach (Marinelli et al. [2019])

E [MPa]	ν [-]	σ_{ci} [MPa]	m_i [-]	m_{ψ_0} [-]	B_m [-]	B_s [-]	B_ψ [-]
8500	0.17	38	10	8	0.017	0.017	0.0035

The results of the parametric studies are illustrated in *Figure 10*, *Figure 11* and *Figure 12* in which the numerical analyses show the effect of the parameters governing the elastic domain and the softening process. Specifically, in *Figure 10* it is possible to observe the effect of the parameters m_i and m_{ψ_0} on the material response by using the SSM approach, which results in an expansion of the initial yield surface and an increase of the peak dilation, respectively. For the sake of brevity, as the parameters m_i and m_{ψ_0} are the same for both formulations, the corresponding parametric analyses are not displayed for the GSM as the results are analogous (i.e., the same mechanical interpretation holds).

Model Performance

Parametric studies

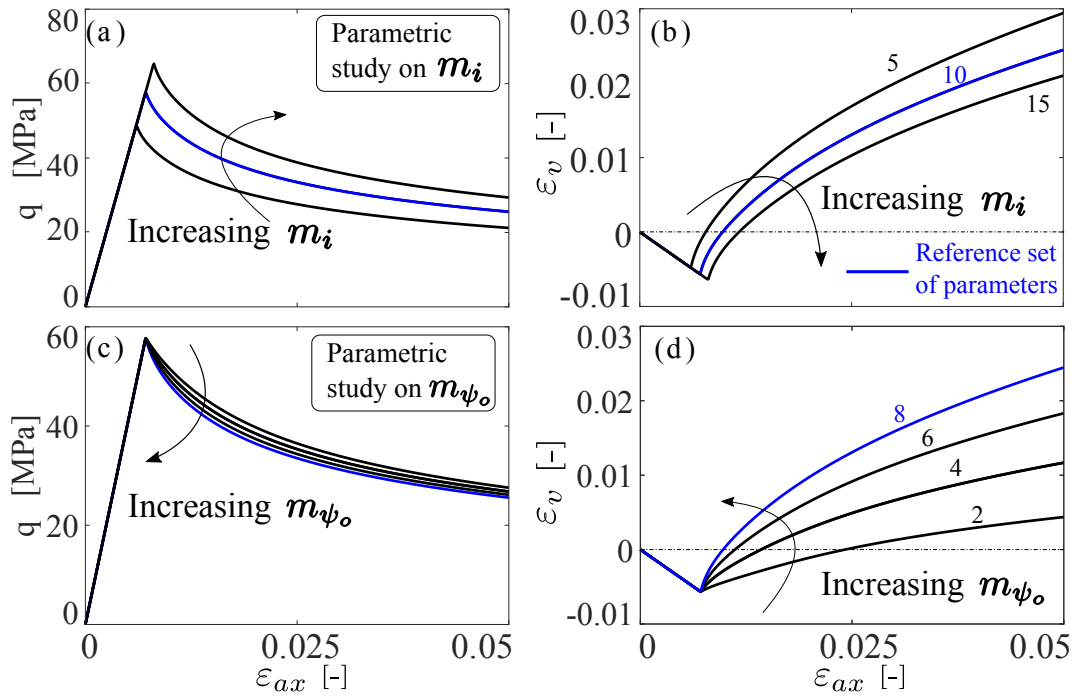


Figure 10: Parametric studies of m_i and m_{ψ_o} for a TXD test at $p_o=5\text{MPa}$

On the contrary, the parameters governing the rate of softening and the rate of dilation are tested with both approaches (i.e. $B_s=B_m$ and B_ψ for SSM, B_{GSI} and F_ψ for GSM). The results have been plotted in the parametric studies of Figure 11 and Figure 12, respectively.

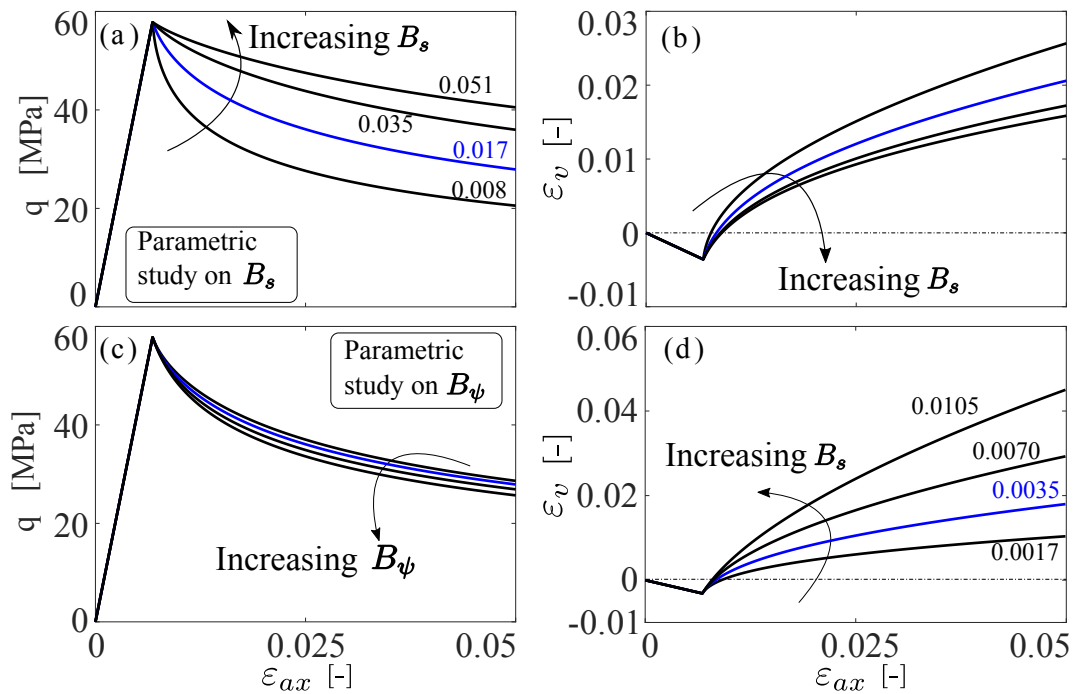


Figure 11: Parametric studies for the parameters $B_s=B_m$ and B_ψ for the SSM for a TXD test at $p_o=5\text{MPa}$

Model Performance

Parametric studies

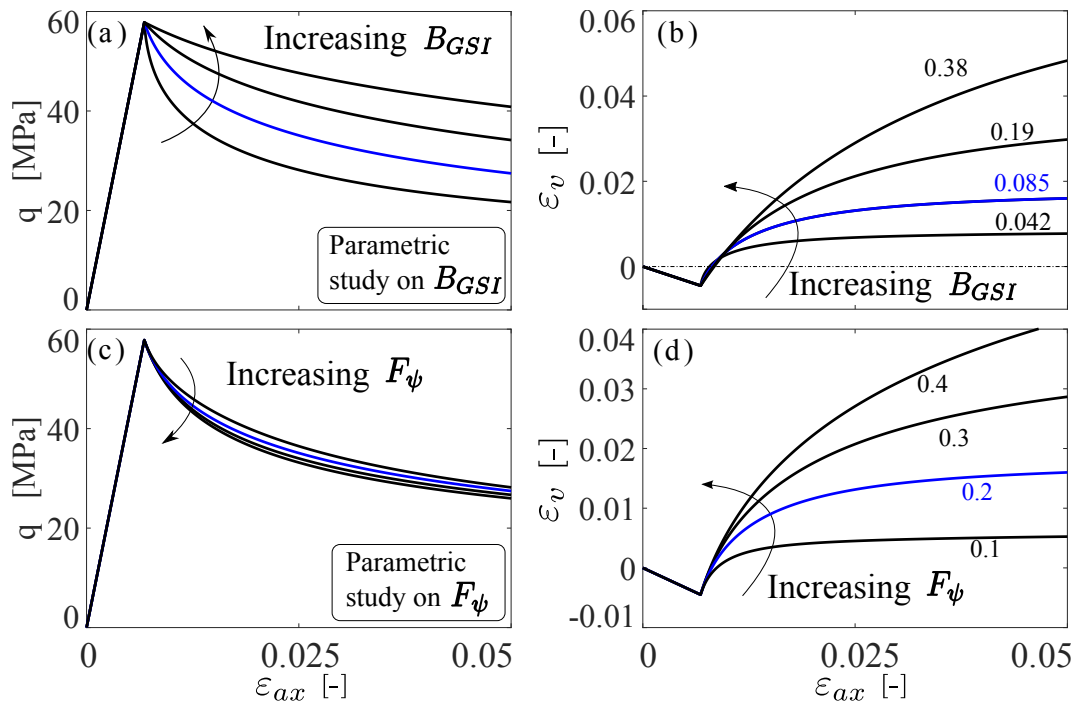


Figure 12: Parametric studies for the parameters B_{GSI} and F_ψ for the GSM for a TXD test at $p_o=5MPa$

Although in terms of softening, the GSM and SSM show a similar qualitative trend for both softening rules (i.e., varying B_s and B_{GSI} the same effect is observed), the main difference can be recognized in the evolution of the volumetric strain behaviour, which tends to reach a non-dilatant state more rapidly in the GSM approach due to the effect of the exponential law. Contrary to B_s , the parameter B_ψ has an important influence on the development of volumetric strain which tends to approach a regime of zero dilation (i.e., lower values of ϵ_v) for lower values of B_ψ .

It is important to remark that the parameters governing the rate of softening and the rate of dilation, (i.e., B_m , B_s , B_ψ or B_{GSI} and F_ψ) should be evaluated through a calibration process which, at least in its former stage, can estimate a first order of magnitude of these parameters. To simplify the calibration process, it is suggested to consider $B_m \equiv B_s$, thus reducing the number of employed parameters within the SSM approach. Since the parameters B_s and B_m (B_{GSI} for the GSM approach) correspond to the specific value of ϵ_p^{eq} at which the hardening variables are reduced by 50%, it is possible to further constrain the admissible values of this parameter between the two limit mechanical response. This is computed by decreasing or increasing the parameter B_j (the subscript j is used to indicate m/s or GSI for the SSM and GSM approaches, respectively).

Large values of B_j results to a quasi-perfectly plastic behaviour, while small values of B_j enable the material response to approach a critical softening regime at the beginning of the plastic flow (Figure 13). Specific values of B_j larger than 10% results to an important reduction of the degradation process, thus approaching a mechanical response characterized by quasi-perfect plasticity. While this scenario does not imply any difficulties during the numerical integration of the constitutive model, the value of B_j corresponding to a critical softening behaviour prevents the definition of the plastic multiplier Λ , thus requiring more complex computational strategies to integrate the constitutive equations for a given time step (Conti et al., 2013 (on page 38)).

To avoid such complexities, an expression to define a lower-bound of this parameter is proposed hereafter for two different stress paths (i.e., triaxial and biaxial compression test). For this purpose, a parametric study has been performed for different values of the material properties (i.e., σ_{ci} , E and m_i) to detect the specific value of B_j (i.e., noted as $B_{j,crit}$) for which the occurrence of critical softening prevents the integration of the material

Model Performance

Parametric studies

response. These results have been reported in *Figure 14* for both softening formulations, thus highlighting the intrinsic dependency between $B_{j,crit}$ and the material properties (i.e., E , σ_{ci} and m_i) during a biaxial test performed without confining pressure.

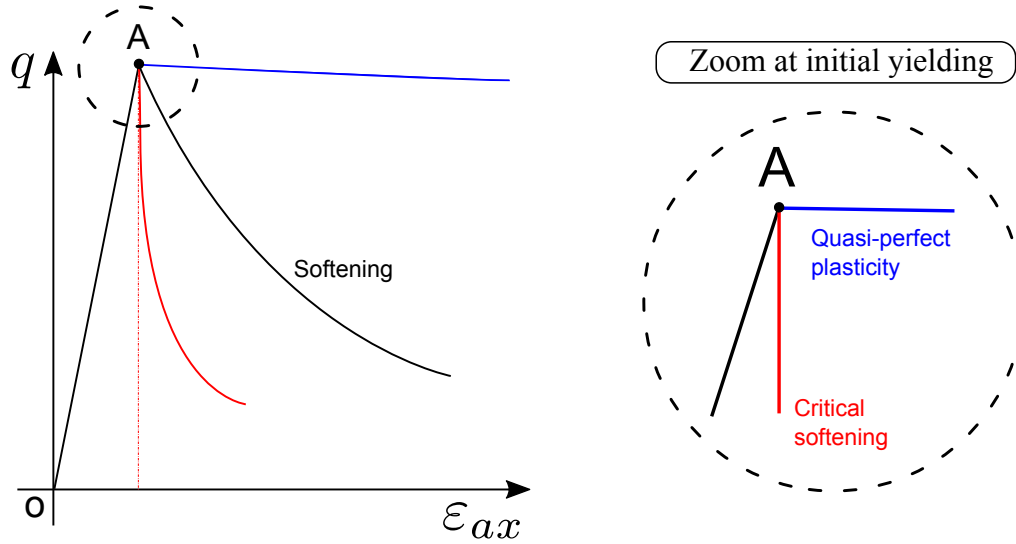


Figure 13: Qualitative sketch of two different limit material response obtained by changing the parameter governing the rate of softening from low to large values.

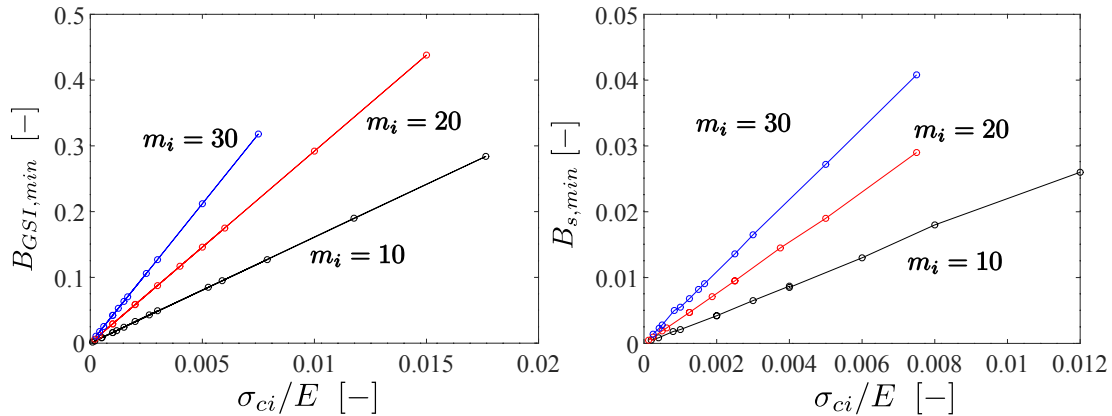


Figure 14: Values of $B_{j,crit}$ corresponding to critical softening behaviour at initial yielding of a drained biaxial test for different values of the material properties.

To generalize the plots shown in *Figure 14*, the results have been interpolated with a linear regression whose equation can be expressed as:

$$B_{j,crit} \rightarrow \begin{cases} B_{j,crit}^s = [C_1^s \cdot m_i + C_2^s] \cdot \left(\frac{\sigma_{ci}}{E}\right) \\ B_{j,crit}^{GSI} = [C_1^{GSI} \cdot m_i + C_2^{GSI}] \cdot \left(\frac{\sigma_{ci}}{E}\right) \end{cases} \quad Eq. [32]$$

where

$B_{j,crit}$ = particular value of B_j corresponding to a critical softening response at first yielding for a specific stress path (*Figure 13*).

Model Performance

Parametric studies

The coefficients C_1^s and C_2^s (or alternatively, C_1^{GSI} and C_2^{GSI}) computed for biaxial stress paths are reported in *Table 2* for both softening formulations where, to extend the applicability of Eq. 32 to other stress paths, the same parametric study has been repeated also by solving triaxial compression tests (i.e., uniaxial compression, UC). It is worth mentioning the fact that for UC, the coefficient C_1 employed in both approaches can be considered neglected with respect to the coefficient C_2 . The different order of magnitude of this coefficient is explained by observing the original HB formulation and by considering that for uniaxial compression tests the influence of the mechanical response on the variability of m_b is deleted by the vanishing value of the confining pressure (i.e., $\sigma_3 = 0$).

Table 2: Values for C_1^s , C_2^s , and C_1^{GSI} and C_2^{GSI} for the SSM and GSM, respectively. These coefficients are obtained by performing drained triaxial (TXD) and biaxial (BXD) stress paths at zero confining pressure.

	C_1^s	C_2^s	C_1^{GSI}	C_2^{GSI}
BXD	0.163	0.564	1.309	3.059
TXD	0.005	0.600	0.0001	12.963

The performance of both softening formulations are plotted in *Figure 15* in which a drained triaxial test performed at 5 MPa of confining pressure has been computed for different initial values of the Geological Strength Index. In these computations also the Young modulus has been considered as a function of the *GSI* according to the formulation proposed by [Hoek and Diederichs \(2006\)](#) (on page 39) which is expressed as:

$$E_{rm} = 100000 \left(\frac{1 - D/2}{1 + e^{(75+25D-GSI_0)/11}} \right) \quad \text{Eq. [41]}$$

Figure 15 highlights a potential mechanical response of the rock mass for which the initial material properties prescribed by GSI_0 have an influence not only on the stiffness and the peak strength but also on the rate of softening employed to reach the residual strength of the material. This figure shows the ability of the model to reproduce the post-peak behaviour of the rock mass through a continuous decay of the material properties along the lines of the post-peak characterization proposed in [Alejano et al. \(2010\)](#) (on page 38).

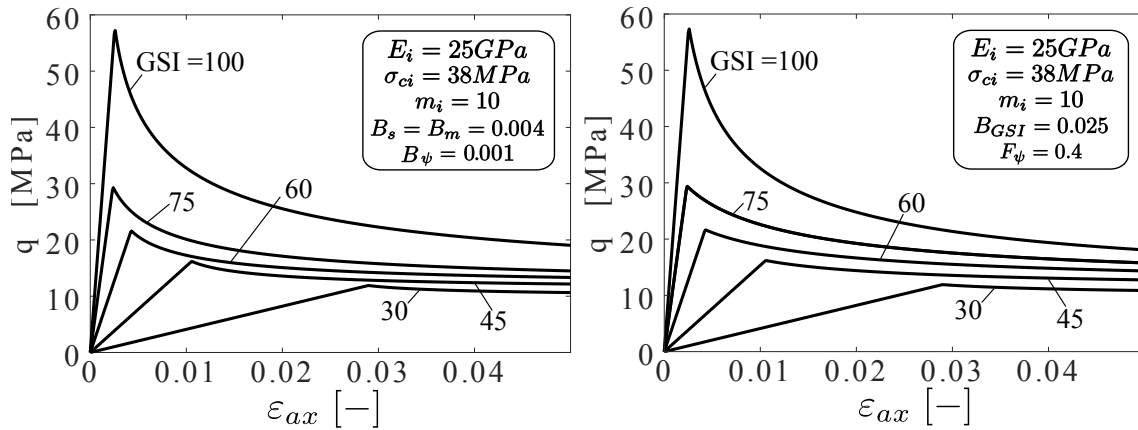


Figure 15: Performance of the proposed models under triaxial compression for different values of the GSI_0 : a) Strength Softening Model (SSM), b) GSI Softening Model (GSM). In both cases a radial confining pressure equal to 5 MPa.

Model Performance

Model Calibration

Model Calibration

To show the performance of the underlying model to simulate the intact rock behaviour under triaxial loading paths (TXD), a first order calibrations for different types of rocks has been performed using the parameters listed in *Table 3*.

Table 3: Parameters used in the calibrations for different types of rock (data after: (a)Bésuelle et al., 2003; (b) Alejano et al., 2012; (c) Santarelli, 1987; (d) Papazoglou, 2018; (e) Wong, 1998)

Rock	p_o [MPa]	E [MPa]	ν [-]	σ_{ci} [MPa]	m_i [Mpa]	m_ψ [-]	B_{GSI} [-]	F_ψ [-]	B_s [-]	B_ψ [-]
Sandstone ^(a)	5	8500	0.19	38	10	8	0.085	0.20	0.017	0.0035
Granite ^(b)	4	21000	0.19	76.59	40.96	25	0.058	0.45	0.011	0.006
Dolomite ^(c)	5	25000	0.2	66	11	10	0.05	0.35	0.005	0.0045
	20	25000	0.2	66	11	9	0.16	0.35	0.012	0.0045
Taffeau ^(d)	0	300	0.2	2.2	9.7	9	0.16	0.35	0.03	0.005
	0.5	300	0.2	2.2	9.7	6	0.16	0.35	0.015	0.01
Shale ^(e)	0.05	90	0.2	2	4	2.2	0.16	0.40	0.018	0.03
	0.25	90	0.2	2	4	1	0.16	0.40	0.025	0.03

The resulting mechanical behaviour is plotted in *Figure 16* and *Figure 17* which show the ability of the HBS model to reproduce the qualitative brittle behaviour of these rocks. It is important to remark that the proposed set of parameters simulates the homogenous behaviour of the material computed at the material point level, thus neglecting the strong non-homogeneous strain-field observed in the experiments (i.e., the strain localization phenomena leading the material to failure). For this reason, although the underlying calibration enables a first order estimation for the value of the model parameters, a rigorous calibration process in the brittle regime should implement an inverse analysis method which compares full-field experimental data with the numerical solution of the experimental test simulated as an IBVP ([El Moustapha, 2014](#) (on page 39); [Besuelle and Lanata, 2017](#) (on page 38)).

Model Performance

Model Calibration

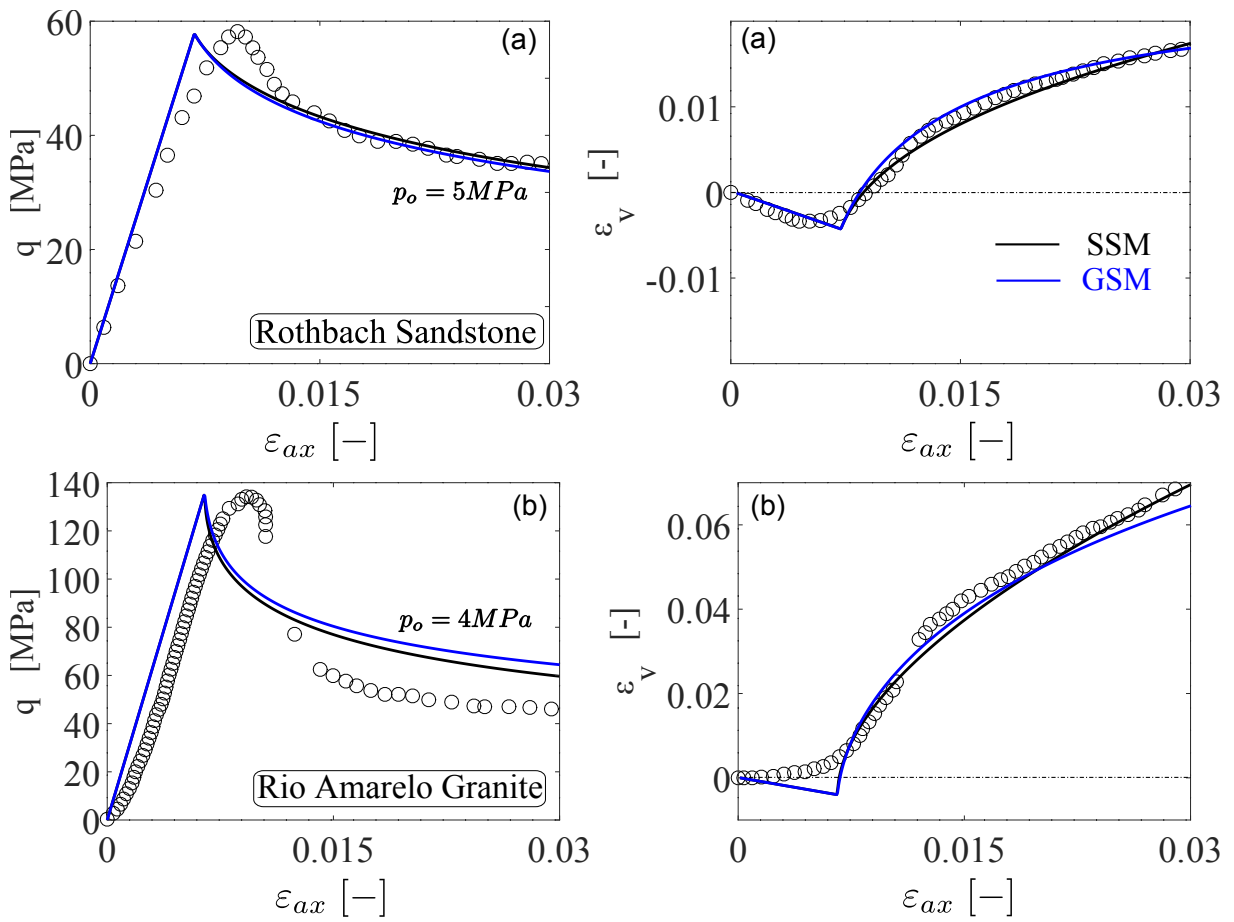


Figure 16: First order calibration 1 for different materials: a) Rothbach Sandstone data after Marinelli et al. (2019); b) Rio Amarelo Granite data after Alejano et al. (2012)

Model Performance

Model Calibration

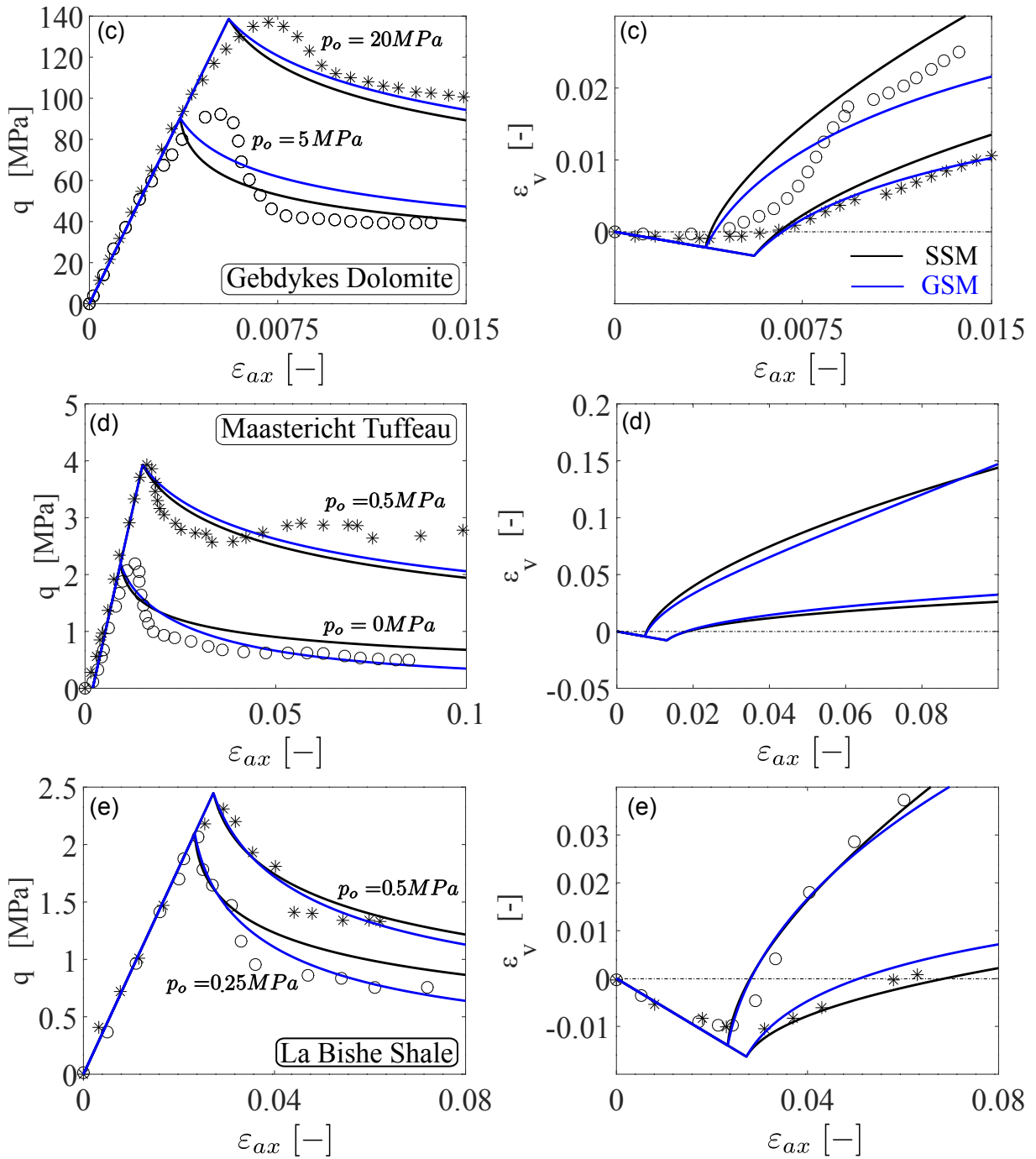


Figure 17: First order calibration 2 for different materials: c) Gebdykes Dolomite data after Santarelli (1987); d) Maastericht Tuffeau data after Papazoglou (2018); e) La Bishe Shale data after Wong (1988).

5

Modeling Strain Localization

Failure mechanisms in geomaterials are often characterized by a rapid concentration of strain in narrow zones which is a phenomenon commonly referred to in literature as *strain localization*. In the brittle/dilatant regime, the development of localized shear bands strongly reduces the global resistance of the mechanical domain, thus leading the engineering geo-structure to failure.

In the framework of numerical analyses, one of the classical problems for modelling the development of shear bands, is the pathological mesh-dependence of the computed solution which implies failure without energy-dissipation ([Pijaudier-Cabot and Bazant, 2017](#) (on page 39)). To avoid this unphysical behaviour an internal length has to be introduced to govern the evolution of the shear band thickness in the post-peak regime of the material response.

In the implemented HBS, to restore the mesh-objectivity of the numerical solution a visco-plastic regularization is considered based on the over-stress theory of [Perzyna \(1966\)](#) (on page 39), thus enabling the introduction of an internal length through a temporal gradient ([Sluys, 1944](#) (on page 39)). Although in this approach a rate-effect is activated during the formation of the shear band, the advantage of this method relies on the straightforward implementation of an implicit integration algorithm which guarantees a readily switch between the elasto-plastic and the visco-plastic version of the same model ([Marinelli and Buscanera, 2019](#) (on page 39)).

Viscous regularization technique

Hereafter, the over-stress approach proposed by [Perzyna \(1966\)](#) (on page 39) is considered to introduce a rate-dependency within the elasto-plastic framework presented in previous sections. In this approach, the increment of the visco-plastic strains is expressed through a viscous nucleus function Φ which represents a measure of plastic violation (i.e., how much the stress state lays outside of the yield surface) and prescribes the magnitude of the strain rate:

$$\dot{\varepsilon}_{ij}^{vp} = \gamma \langle \Phi(f) \rangle \left(\frac{\partial g}{\partial \sigma_{ij}} \right), \quad \Phi = \frac{f}{\sigma_{ci}} \quad \text{Eq. [34]}$$

where

$$\begin{aligned} \gamma &= \text{Fluidity (i.e., the inverse of the viscosity).} \\ \langle \cdot \rangle &= \text{McCauley brackets.} \end{aligned}$$

The purpose of the viscous regularization method is to set the value of the fluidity γ to approach an inviscid-like behaviour at the material point and, at the same time, to introduce an internal length through a temporal gradient. In other words, although in some engineering problems it is crucial to calibrate the value of the fluidity to mimic the rate-effects resulting from the fast-dynamics features of the boundary conditions (see for instance [Manouchehrian and Cai, \[2017\]](#) (on page 39)), in our context the fluidity has the only goal of regularizing a strain localization problem.

Modeling Strain Localization

Strain localization analysis

An example of the aforementioned is illustrated on *Figure 18* where a uni-axial compression test is performed for different values of γ and for a given rate loading. In this figure, it is possible to observe how the rate-dependent model approaches the elasto-plastic behaviour by increasing the value of the corresponding fluidity. Once the fluidity has been constrained to reduce the rate-dependent effects at the material point level, this parameter can be used to control the shear band thickness, thus providing a regularization effect in the numerical problem. In the next section, the performance of the viscous regularization technique will be inspected by solving plane strain compression tests, for which the mesh objectivity will be detailed by showing the invariance of both the global strength and shear band thickness with the spatial discretization of the sample.

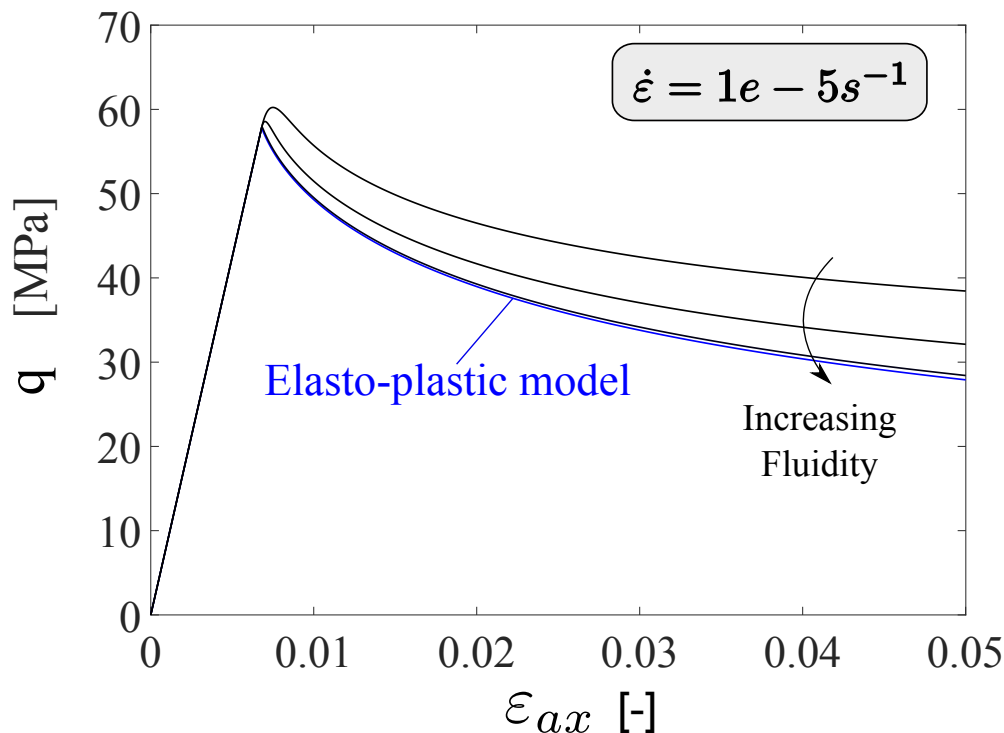


Figure 18: Influence of the fluidity γ on the rate-dependent response of HBS model: Convergence of the visco-plastic model to the elasto-plastic model for increasing values of the fluidity γ .

Strain localization analysis

To investigate the performance of the viscous regularization method, a set of plane strain compression tests have been computed with PLAXIS 2D code. The details of this Initial Boundary Value Problems (IBVP) are depicted in *Figure 18*, where the grey area represents a particular zone in which the material strength is reduced with the purpose of triggering the formation of the shear band from the bottom-left corner of the sample.

The parameters used for these numerical analyses are the same reported in *Table 1* for Rothbach sandstone with the only exception of the uni-axial compression strength defined in the grey area which has been reduced to 37MPa.

Modeling Strain Localization

Strain localization analysis

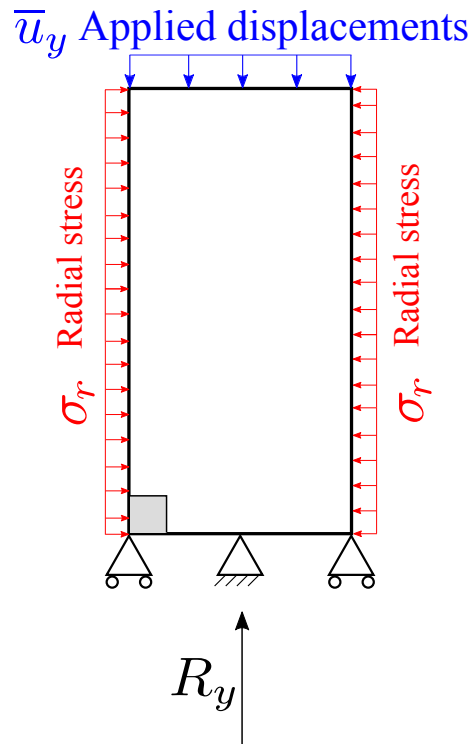


Figure 19: Initial and boundary conditions used to compute a drained compression test in plane strain compression (i.e., a biaxial test (BXD)). The grey area represents a zone characterized by reduced properties (i.e., $\sigma_{ci}=37$ MPa) which have been selected to trigger the strain localization phenomenon, while the variable R_y stands for the global reaction of the sample.

Before showing the beneficial effect of a rate-dependent formulation, it is worth illustrating an example of numerical solutions obtained with the elasto-plastic version of this model thus emphasizing how the mesh discretization can affect the numerical solution. For this purpose, the same IBVP (i.e., a compression test in plane strain conditions) has been solved with a different number of elements and the results expressed in Figure 20 where the evolution of the total reaction R_y has been plotted as a function of the applied displacement. The mesh sensitivity of the sample response is explained by observing the spatial distribution of the Gauss points in plastic loading (i.e., the red points inside the elements of the sample) which results from a different number of elements (NEL) employed in the FE computations.

As a matter of fact, the lack of an internal length in the elasto-plastic model unable to prescribe the shear-band thickness which is intrinsically given in the numerical problem by the size of the element. As a consequence, due to this inherent dependence between the element size and the band thickness, a refinement of the mesh involves a more intense dissipation process, thus explaining the sharper decrease of resistance of the sample discretized with a larger number of elements. It is important to remark that, when the element size is too small, the model is not able to satisfy the global convergence due to the large values of the strain gradient computed inside the shear band. This is illustrated by the green line of Figure 20 in which the computation stops before the 2% of applied displacements.

Modeling Strain Localization

Strain localization analysis

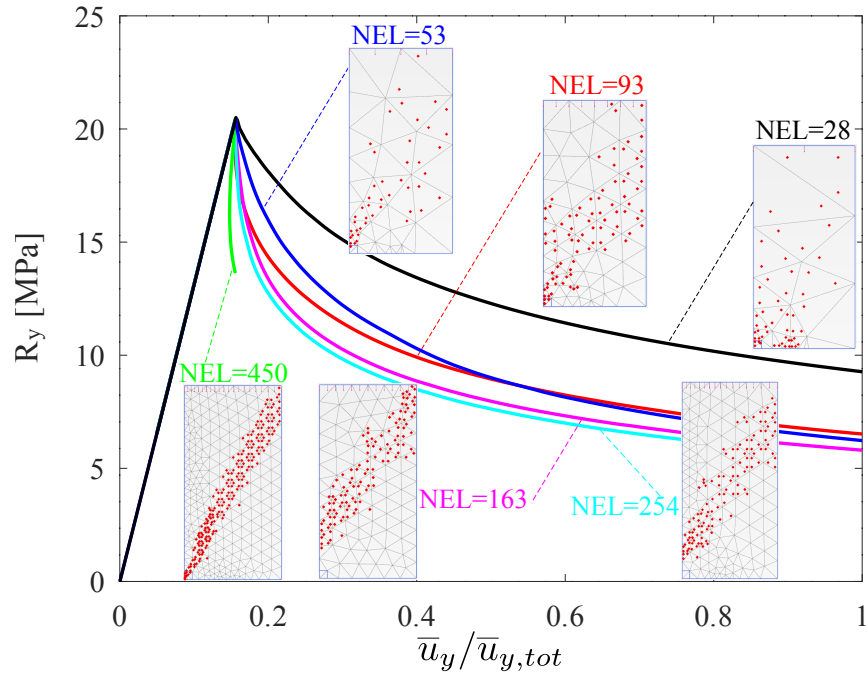


Figure 20: Vertical reaction of a drained biaxial test performed with a radial stress of $\sigma_r=1$, MPa and with a different number of elements (NEL). The red squares inside the elements indicate Gauss points in plastic loading.

To show the regularization effect introduced by the rate dependent model, two drained biaxial tests have been performed with two different values of fluidity. These computations have been performed by enforcing a rate of displacement equal to 0.001mm/s and a radial stress of 5 MPa. The results are plotted in Figure 21 where the same IBVP is repeated for different meshes thus showing the convergence of the solution with respect to the mesh density (i.e., for an increasing number of elements, R_y tends to converge to the same curve).

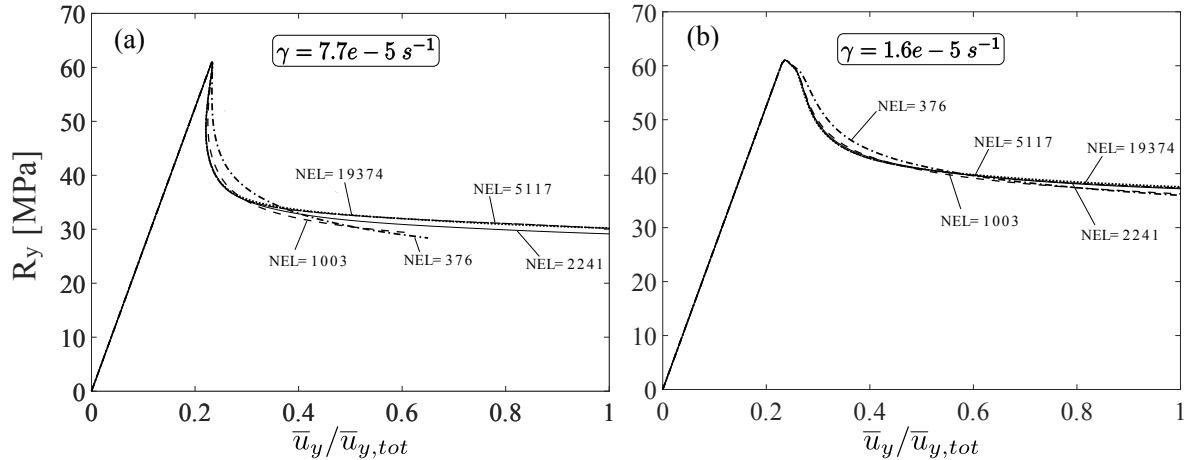


Figure 21: Evolution of the total vertical reaction for different meshes and two values of fluidity. Computations performed by prescribing a radial confinement equal to 5 MPa and a rate of displacement of 0.001mm/s .

Furthermore, to better identify the formation of the shear band during the time steps, the spatial distribution of the Gauss points in a plastic state and the corresponding shear strain are plotted in Figure 22 for the two different values of the fluidity which readily emphasize the different effect on the band thickness for the specific value of γ .

Modeling Strain Localization

Strain localization analysis

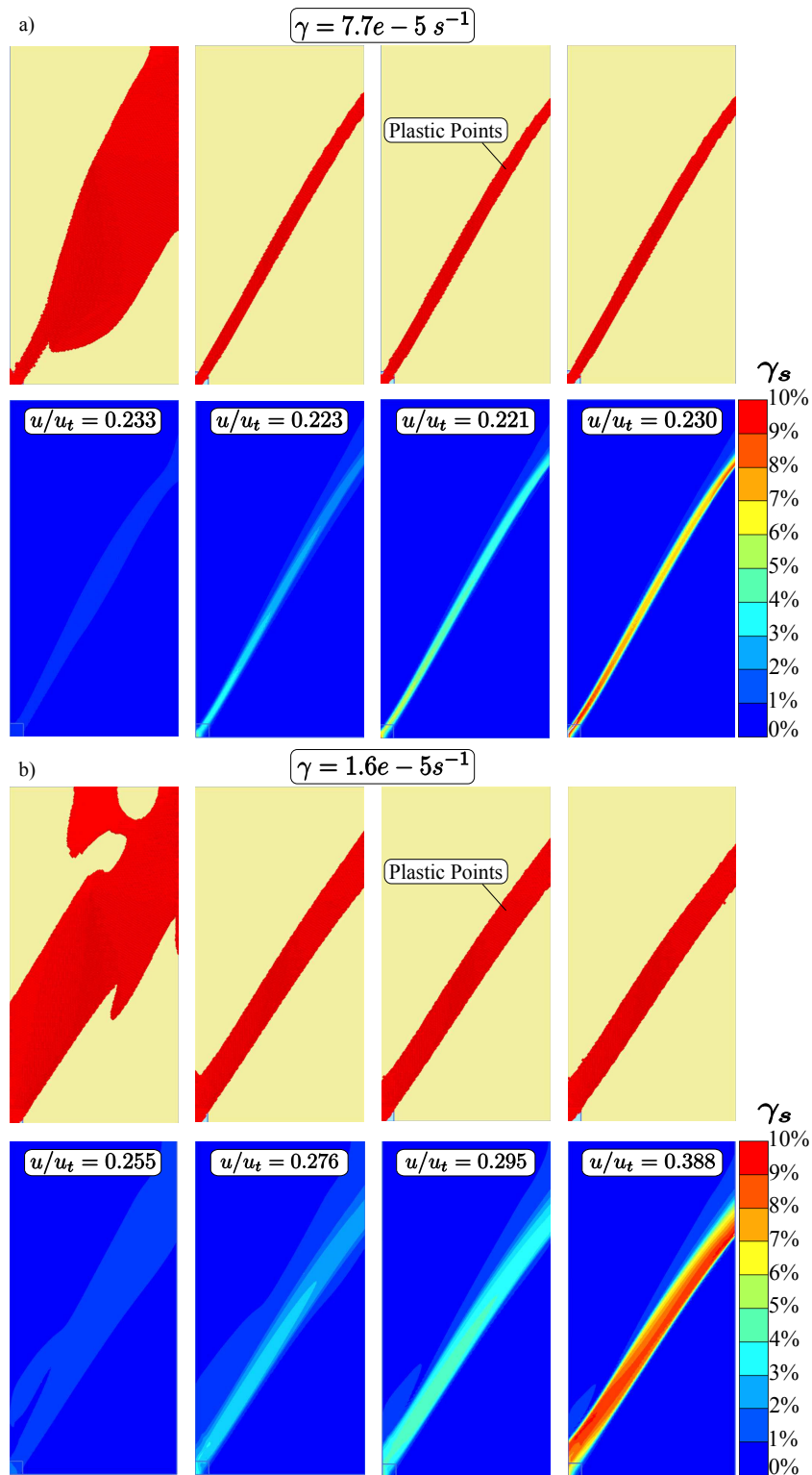


Figure 22: a) Plastic point and shear strain for four steps of the computation performed with $\gamma=7.7E-5/s$ corresponding to a band width of 4mm b) Plastic point and shear strain for four steps of the computation performed with $\gamma=1.6E-5/s^{-1}$ corresponding to a band width of 9mm.

Modeling Strain Localization

Strain localization analysis

Lower values of fluidity correspond to thinner thickness values of the shear band (i.e., the thickness of the shear band is proportional to the viscosity). The influence of the internal length enforced through the parameter γ is also detailed in *Figure 23*, in which the biaxial tests have been repeated from a fluidity value of $\gamma=1.3E-5s^{-1}$ to $\gamma=2.3E-4s^{-1}$, thus showing the structural effect of the band thickness on the global rate of softening of the sample. It is worth remarking that the computations presented in this sections have been calculated by selecting the maximum number of iterations equal to 250.

As a matter of fact, at the beginning of the post-peak regime, when the material starts softening the Newton-Raphson algorithm requires a higher iteration number to reach a converged solution. This particular behavior of the convergence trend is further accentuated by the value of the tolerated error which has been selected equal to 0.001 to guarantee a satisfactory precision of the computations. All the numerical input employed in these computations are listed here below:

- Tolerated error: 0.001
- Max load fraction per step: 0.02
- Over-relaxation factor: 1.2
- Max number of iterations: 250
- Desired min number of iterations: 6
- Desired max number of iterations: 25
- Arc-length control type: On

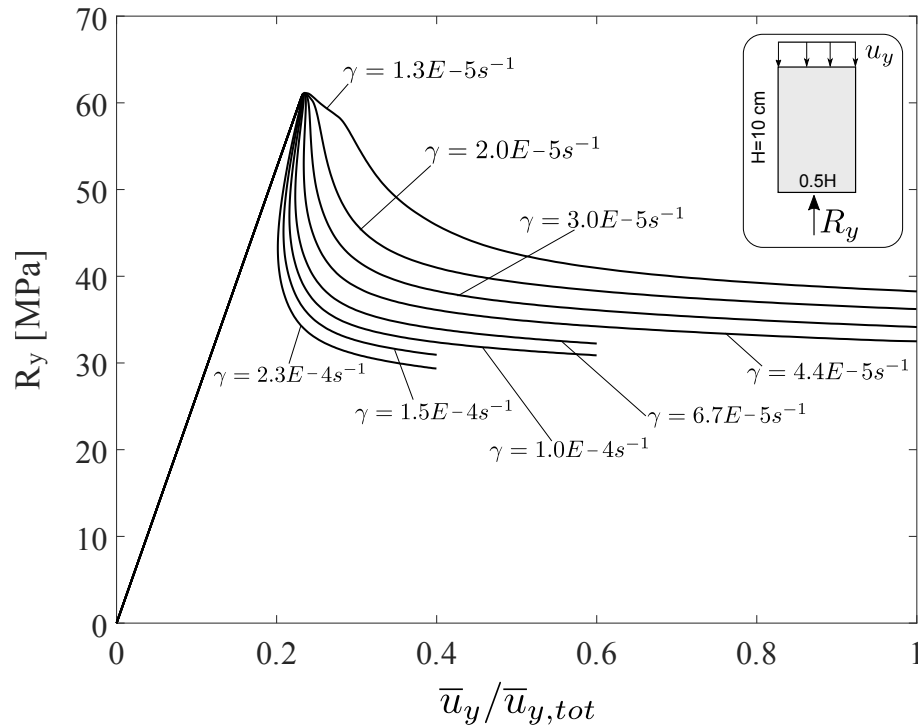


Figure 23: Vertical reaction of a drained biaxial test performed with a radial stress of $\sigma_r=5$, MPa for different fluidity values γ .

6

Simulation of Tunnel Excavation

To compare the solution of the implemented model with the analytical solution proposed by Carranza-Torres (2004) (on page 38), perfect plastic conditions have been taken account. Specifically, the parameters reported in Table 1 have been selected with the only difference that zero dilation angle is considered. The results are shown in Figure 24 where the displacement at the top of the tunnel have been plotted against the deconfined stress p_i . In this figure, the development of shear bands around the tunnel at the end of the unloading phase is also illustrated for different time steps. By observing this figure, it is worth noting that point 2 represents the end of the axisymmetric solution and the beginning of the shear bands propagation.

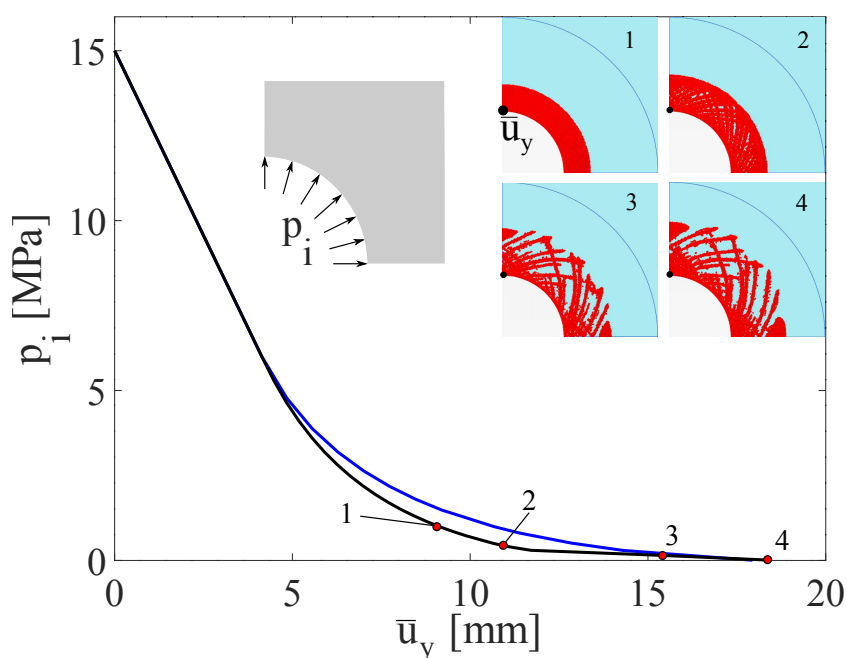


Figure 24: Ground Reaction Curve (GRC) under perfect plastic conditions modeled with the generalized HB criterion closed form solution from Carranza-Torres (2004) (blue line) and the viscous-regularized solution (black line).

To emphasize the effect of strain softening, a comparison of the Ground Reaction Curve (GRC) for different initial conditions of a limestone rock mass (data after Alejano et al., 2010 (on page 38)) is shown in Figure 25 where the parameters reported in Table 4 have been taken into account. These computations have been performed with three different set of parameters with the purpose of highlighting specific constitutive features of the model: (i) model A (perfect plasticity), (ii) model B (HBS with constant dilation), (iii) model C (HBS with non-linear dilation). It is worth remarking that in Figure 25 the non-smooth trend of the convergence-confinement curve results from the development of localized strain around the tunnel whose formulation involves an irregular profile of the deformation field.

Simulation of Tunnel Excavation

Table 4: Characterization of limestone rock masses ($m_i = 10$, $\sigma_{ci} = 75\text{MPa}$) for different rock qualities (from Alejano et al., 2010) applied to the models: A-Perfect plastic, B-Strain softening with constant dilation and C-Strain softening with variable dilation

Model	Parameter	GSI = 75	GSI = 60	GSI = 50	GSI = 40	GSI = 25
A, B, C	m_{b_o}	4.090	2.397	1.677	1.173	0.687
A, B, C	s_o	0.062	0.0117	0.0039	0.0013	0.0002
B, C	m_{b_r}	1.173	0.981	0.821	0.737	0.687
B, C	s_r	0.0013	0.0007	0.0004	0.0003	0.0002
B, C	$B_\psi B_m$	0.01	0.01	0.01	0.01	0.01
A, B	$m_{\psi_{const}}$	0.718	0.312	0.166	0.060	0.000
C	m_{ψ_o}	1.225	0.587	0.330	0.156	0.000
C	m_{ψ_r}	0.000	0.000	0.000	0.000	0.000
C	B_ψ	0.001	0.001	0.001	0.001	0.001

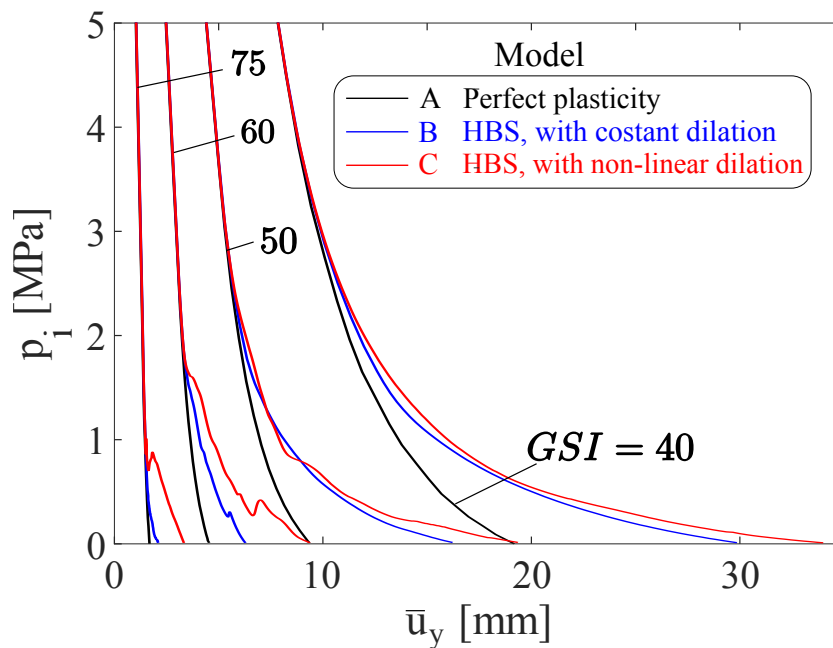


Figure 25: Ground reaction curves (GRC) for different values of GSI with different models: A- perfect plastic model (black lines), B- strain softening model with constant dilation angle (blue lines) and C- strain softening model with variable dilation model (red lines). For all computations $\gamma = 15d^{-1}$.

Simulation of Tunnel Excavation

Furthermore, the presented formulation has been also compared with other approaches which introduce a softening rule within a HB framework (i.e., [Alejano et al., 2010](#) (on page 38) and [Ranjbarnia et al., 2015](#) (on page 39)). The results are plotted in *Figure 26* and show a similar trend of behavior in terms of GRC.

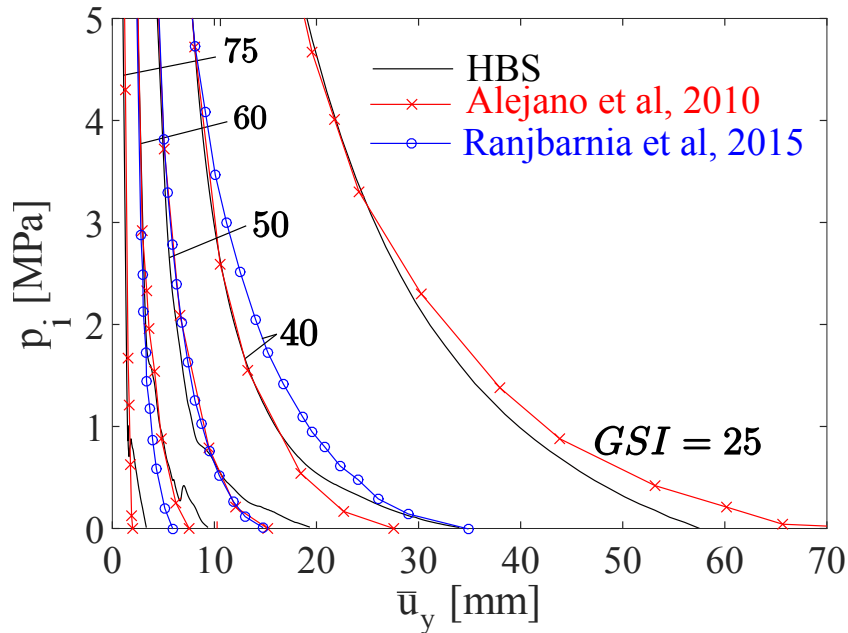


Figure 26: Ground reaction curves (GRC) for different values of GSI comparing the HBS model to the models proposed by Alejano et al. (2010) and Ranjbarnia et al. (2015).

In addition, the effect of rate dependence is evaluated by running tests varying the fluidity γ as shown in *Figure 27*. In this case, the parameter γ controls the structural effect on the response. In previous computations a fluidity $\gamma = 15 \text{ d}^{-1}$ has been used.

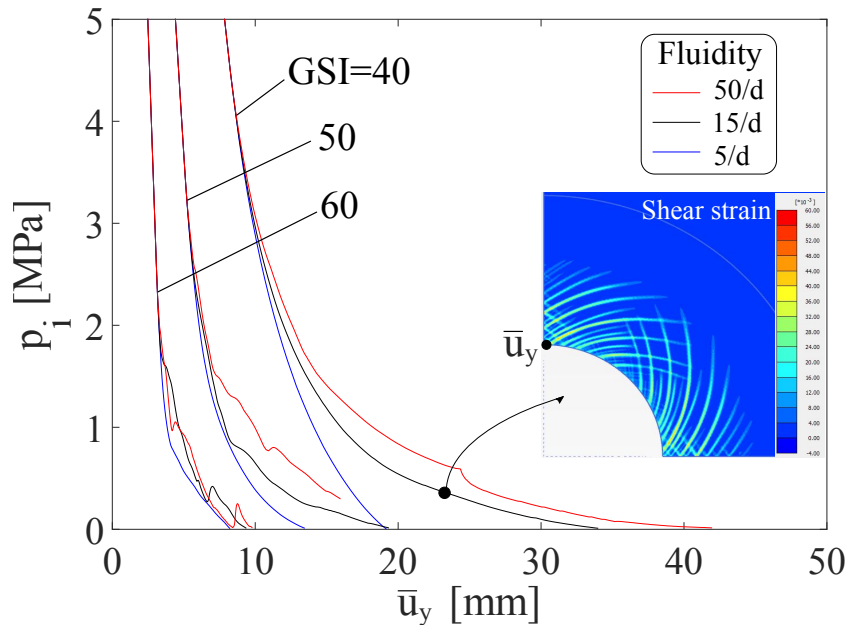


Figure 27: Ground reaction curves (GRC) for different values fluidity (γ) showing the effect of rate dependence of the model.

Simulation of Tunnel Excavation

Case study: Donking-Morien Tunnel

Case study: Donking-Morien Tunnel

The access tunnel for the Donking-Morien coal mine in Cape Breton Island, Nova Scotia, Canada was driven to a maximum depth of 200m below the seabed in a layered sedimentary rock dipping 10°. This tunnel has been monitored with extensometer measurements in several sections and back analyses performed in [Pelli et al. \(1991\)](#) (on page 39) and in [Walton et al. \(2014\)](#) (on page 40) specifically at chainage 2996 m due to the quality of the data and lack of geological interfaces.

The field stress in the tunnel, estimated by [Walton \(2014\)](#) (on page 40), is $\sigma_v = 5 \text{ MPa}$ and $\sigma_h = 10 \text{ MPa}$. Laboratory tests have reported UCS ranging from 15 MPa to 63 MPa with a mean value of 36 MPa and a Young's modulus between 4 GPa and 15 GPa, while extensometer measurements show a modulus of 5.6 GPa at chainage 2996. The plastic zone depth reported by [Pelli et al. \(1991\)](#) (on page 39) is 1,8 m in the crown. [Corkum et al. \(2012\)](#) (on page 38) reports a *GSI* between 70 and 80 for the selected material.

This section of the tunnel was modeled with the HBS with the parameters set to the mean values reported by laboratory experiments and in-situ measurements. The numerical analyses show the capabilities of the model to provide reliable estimations for design purposes as shown in *Figure 28*. Specifically, *Figure 28(a)* shows a cross section of the vertical displacements in the crown compared with extensometer measurements, as well as the GRC (*Figure 28(b)*) and the spatial distribution of the plastic zone (*Figure 28(c)*). Although the model underestimates the plastic zone depth, the observed displacements and the plastic modulus are consistent with the measurements.

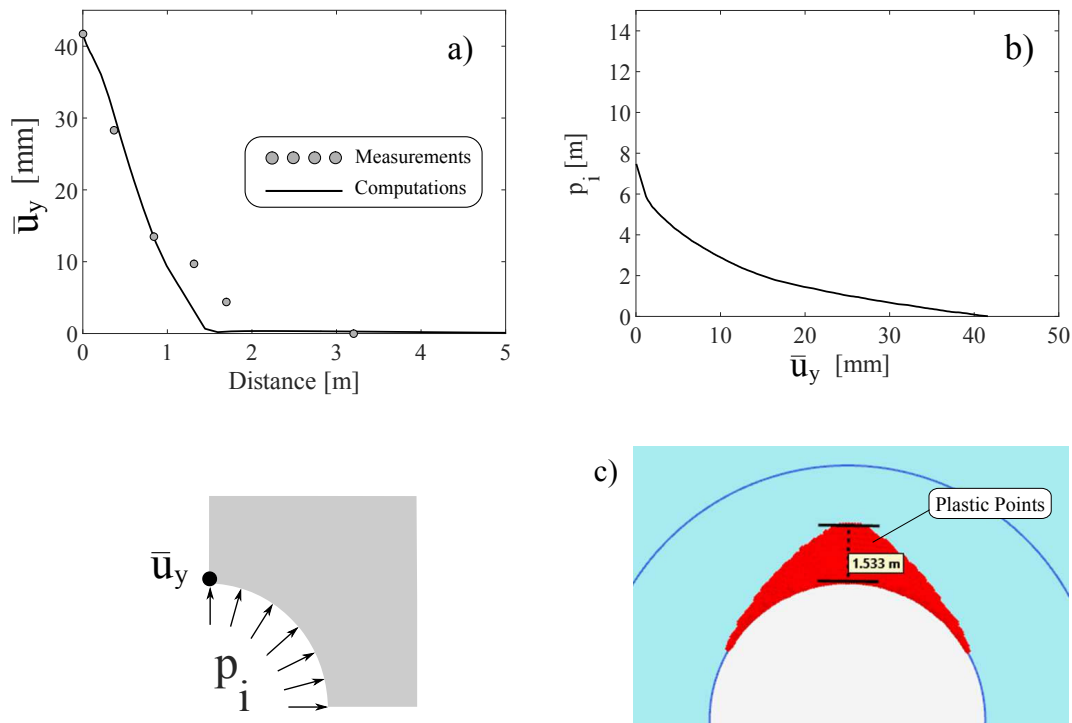


Figure 28: Results of the computation for the Donking Morien tunnel. a) Cross section of vertical displacements at the crown, b) GRC, c) the plastic zone evolution.

7

References

1. Alejano, L. and Alonso, E. (2005). Considerations of the dilatancy angle in rocks and rock masses. *International Journal of Rock Mechanics and Mining Sciences*, 42(4):481 - 507.
2. Alejano, L., Alonso, E., Rodríguez-Dono, A., and Fernández-Manín, G. (2010). Application of the convergence-confinement method to tunnels in rock masses exhibiting Hoek-Brown strainsoftening behaviour. *International Journal of Rock Mechanics and Mining Sciences*, 47(1):150 - 160.
3. Alejano, L., Arzua, J., Alonso, E., et al. (2012). Impact of post-failure rock mass behavior on excavation response. In *46th US Rock Mechanics/Geomechanics Symposium*. American Rock Mechanics Association.
4. Alonso, E., Alejano, L., Varas, F., Fdez-Manin, G., and Carranza-Torres, C. (2003). Ground response curves for rock masses exhibiting strain-softening behaviour. *International journal for numerical and analytical methods in geomechanics*, 27(13):1153-1185.
5. Barnichon, J.-D. (1998). *Finite Element Modelling in Structural and Petroleum Geology*. PhD thesis, Université de Liège Faculté des Sciences Appliquées.
6. Bazant, Z., Belytschko, T., and Chang, T. (1984). Continuum theory for strain softening. *Journal of Engineering Mechanics*, 110(12):1666-1692.
7. Besuelle, P. and Lanata, P. (2017). Emergence of strain localization in porous rocks characterized by full-field measurement in plane strain condition. In Papamichos, E., Papanastasiou, P., Pasternak, E., and Dyskin, A., editors, *Bifurcation and Degradation of Geomaterials with Engineering Application*, pages 25-31, Cham. Springer International Publishing.
8. Bésuelle, P., Baud, P., and Wong, T.-F. (2003). Failure mode and spatial distribution of damage in rothbach sandstone in the brittle-ductile transition. In Kümpel, H.-J., editor, *Thermo- Hydro-Mechanical Coupling in Fractured Rock*, Pageoph Topical Volumes, pages 851-868. Birkhäuser Basel.
9. Cai, M., Kaiser, P., Tasaka, Y., and Minami, M. (2007). Determination of residual strength parameters of jointed rock masses using the GSI system. *International Journal of Rock Mechanics and Mining Sciences*, 44(2):247 - 265.
10. Cai, M., Kaiser, P., Uno, H., Tasaka, Y., and Minami, M. (2004). Estimation of rock mass deformation modulus and strength of jointed hard rock masses using the GSI system. *International Journal of Rock Mechanics and Mining Sciences*, 41(1):3 - 19.
11. Carranza-Torres, C. (2004). Elasto-plastic solution of tunnel problems using the generalized form of the Hoek-Brown failure criterion. *International Journal of Rock Mechanics and Mining Sciences*, 41(SUPPL. 1):1-11
12. Collin, F. (2003). *Couplages thermo-hydro-mécaniques dans les sols et les roches tendres partiellement saturés*. PhD thesis, Université de Liège, Faculté de Science Appliquées.
13. Conti, R., Tamagnini, C., and DeSimone, A. (2013). Critical softening in cam-clay plasticity: Adaptive viscous regularization, dilated time and numerical integration across stress-strain jump discontinuities. *Computer Methods in Applied Mechanics and Engineering*, 258:118 - 133.
14. Corkum, A., Lorig, L., DeGagne, D., et al. (2012). Continuum representation of brittle rock failure bulking-induced displacements around tunnels. In *46th US Rock Mechanics/Geomechanics Symposium*. American Rock Mechanics Association.

References

15. Crowder, J. and Bawden, W. (2004). Review of post-peak parameters and behaviour of rock masses: current trends and research. Rocnews, fall.
16. El Moustapha, K. (2014). Identification de lois de comportement enrichies pour les géomatériaux en présence d'une localisation de la déformation. PhD thesis, Université de Grenoble, *Laboratoire 3SR*, Equipe GDR.
17. Hoek (1968). Brittle failure of rock. Stagg KG.
18. Hoek, E. and Brown, E. (1997). Practical estimates of rock mass strength. *International Journal of Rock Mechanics and Mining Sciences*, 34(8):1165 - 1186.
19. Hoek, E. and Brown, T. (1980). Underground excavations in in rock. CRC Press. Hoek, E. and Diederichs, M. S. (2006). Empirical estimation of rock mass modulus. *International journal of rock mechanics and mining sciences*, 43(2):203-215.
20. Hoek, E. and Diederichs, M. S. (2006). Empirical estimation of rock mass modulus. *International journal of rock mechanics and mining sciences*, 43(2):203-215.
21. Jiang, H. (2017). A failure criterion for rocks and concrete based on the Hoek-Brown criterion. *International Journal of Rock Mechanics and Mining Sciences*, 95:62 - 72.
22. Jiang, H. and Zhao, J. (2015). A simple three-dimensional failure criterion for rocks based on the Hoek-Brown criterion. *Rock Mechanics and Rock Engineering*, 48(5):1807-1819.
23. Manouchehrian, A. and Cai, M. (2017). Analysis of rockburst in tunnels subjected to static and dynamic loads. *Journal of Rock Mechanics and Geotechnical Engineering*, 9(6):1031-1040.
24. Marinelli, F. and Buscarnera, G. (2019). A generalized backward Euler algorithm for the numerical integration of a viscous breakage model. *International Journal for Numerical and Analytical Methods in Geomechanics*, 43(1):3-29.
25. Marinelli, F., Zalamea, N., Vilhar, G., Brasile, S., Cammarata, G., and Brinkgreve, R. (2019). Modeling of brittle failure based on Hoek & Brown yield criterion: parametric studies and constitutive validation. In *53rd US Rock Mechanics/Geomechanics Symposium*
26. Marinos, V., Marinos, P., and Hoek, E. (2005). The geological strength index: applications and limitations. *Bulletin of Engineering Geology and the Environment*, 64(1):55-65.
27. Papazoglou, A. (2018). An experimental study of localized compaction in high porosity rocks: the example of Tuffeau de Maastricht. PhD thesis, Grenoble Alpes.
28. Pelli, F., Kaiser, P., and Morgenstern, N. (1991). An interpretation of ground movements recorded during construction of the Donkin-Morien tunnel. *Canadian Geotechnical Journal*, 28(2):239-254.
29. Perzyna, P. (1966). Fundamental problems in viscoplasticity. *Advances in Applied Mechanics*, 9:243-377.
30. Pijaudier-Cabot, G. and Bazant, Z. P. (1987). Nonlocal damage theory. *Journal of Engineering Mechanics ASCE*, 113:1512-1533.
31. Rahjoo, M., Eberhardt, E., et al. (2016). A simplified dilation model for modeling the inelastic behavior of rock. In *50th US Rock Mechanics/Geomechanics Symposium*. American Rock Mechanics Association.
32. Ranjbarnia, M., Fahimifar, A., and Oreste, P. (2015). Analysis of non-linear strain-softening behaviour around tunnels. *Proceedings of the Institution of Civil Engineers-Geotechnical Engineering*, 168(1):16-30.
33. Ribacchi, R. (2000). Mechanical tests on pervasively jointed rock material: insight into rock mass behaviour. *Rock mechanics and rock engineering*, 33(4):243-266.
34. Rudnicki, J. and Rice, J. (1975). Conditions for the localization of deformation in pressure-sensitive dilatant materials. *Journal of the Mechanics and Physics of Solids*, 23(6):371 - 394.
35. Santarelli, F. J. (1987). Theoretical and experimental investigation of the stability of the axisymmetric wellbore. PhD thesis.
36. Sluys, L.J. (1994). Wave propagation, localization and dispersion in softening solids. PhD thesis.
37. Vermeer, P. A. and De Borst, R. (1984). Non-associated plasticity for soils, concrete and rock. *HERON*, 29 (3), 1984.

References

38. Walton, G. and Diederichs, M. (2015). A new model for the dilation of brittle rocks based on laboratory compression test data with separate treatment of dilatancy mobilization and decay. *Geotechnical and Geological Engineering*, 33(3):661-679.
39. Walton, G., Diederichs, M., Alejano, L., and Arzúa, J. (2014). Verification of a laboratory-based dilation model for in situ conditions using continuum models. *Journal of Rock Mechanics and Geotechnical Engineering*, 6(6): 522-534.
40. Wong, R. (1998). Swelling and softening behaviour of la biche shale. *Canadian Geotechnical Journal*, 35(2): 206-221.
41. Zhao, X. and Cai, M. (2010). Influence of plastic shear strain and confinement-dependent rock dilation on rock failure and displacement near an excavation boundary. *International Journal of Rock Mechanics and Mining Sciences*, 47(5):723 - 738.
42. Zou, J.-f., Zuo, S.-q., and Xu, Y. (2016). Solution of strain-softening surrounding rock in deep tunnel incorporating 3d Hoek-Brown failure criterion and -ow rule. *Mathematical Problems in Engineering*.

A

Appendix

Table 5: Range of values for σ_{ci} classified according to the different type of rocks.

Rock Material	Resistance classification	<i>Range of Range of σ_{ci} [kN/m²]</i>
Chert, diabase, fresh basalt, gneiss, granite, quartzite	Only chipping is possible with a geological hammer	0 - 250.0E3
Amphibolite, basalt gabbro, gneiss, granodiorite, limestone, marble, rhyolite, sandstone, tuff	Fracturing requires many blows of a geological hammer	100.0E3 - 250.0E3
Limestone, marble, phyllite, sandstone, schist, shale	Fracturing requires more than one blow of a geological hammer	50.0E3 - 100.0E3
Claystone, coal, concrete, schist, shale, siltstone	Fracturing is possible with a single blow from a geological hammer, but cannot be scraped or peeled with a pocket knife	25.0E3 - 50.0E3
Chalk, potash, rocksalt	Firm blow with the point of a geological hammer leaves shallow indentation; peeling with a pocket knife is possible, but difficult	5000 - 25.0E3
Highly weathered or altered rock	Firm blow with the point of a geological hammer leads to crumbling; peeling with a pocket knife is possible	1000 - 5000
Stiff fault gouge	Thumbnail leaves indentation	250 - 1000

Appendix

Table 6: Values of the parameter m_i for different type of rocks. The following nomenclature is used in the Table to indicate the grain size characteristics of the rock: VC (very course), CO (course), ME (medium), FI (fine), VF (very fine). The type of rock is indicated as: IG (igneous), EE (metamorphic), SE (sedimentary).

Rock	$m_i \pm \Delta m_i$	Rock	$m_i \pm \Delta m_i$
Agglomerate (IG, CO)	19 ± 3	Amphibolite (EE, ME)	26 ± 6
Andesite (IG, ME)	25 ± 5	Anhydrite (SE, FI)	12 ± 2
Basalt (IG, FI)	25 ± 5	Breccia (IG)	19 ± 5
Breccia (SE)	19 ± 5	Chalk (SE, VF)	7 ± 2
Claystone (SE, VF)	4 ± 2	Conglomerates (SE, CO)	21 ± 3
Cristalline limestone (SE, CO)	12 ± 3	Dacite (IG, FI)	25 ± 3
Diabase (IG, FI)	15 ± 5	Diorite (IG, FI)	25 ± 5
Dolerite (IG, ME)	16 ± 5	Dolomites (SE, VF)	9 ± 3
Gabbro (IG, CO)	27 ± 3	Gneiss (EE, FI)	28 ± 5
Granite (IG, CO)	32 ± 3	Granodiorite (IG, CO/ME)	29 ± 3
Graywackes (SE, FI)	18 ± 3	Gypsum (SE, ME)	8 ± 2
Hornfels (EE, ME)	19 ± 4	Marble (EE, CO)	9 ± 3
Marls (SE, VF)	7 ± 2	Metasandstone (EE, ME)	19 ± 3
Micritic limestones (SE, FI)	9 ± 2	Migmatite (EE, CO)	29 ± 3
Norite (IG, CO/ME)	20 ± 5	Obsidian (IG, VF)	19 ± 3
Peridotite (IG, VF)	25 ± 5	Phyllite (EE, FI)	7 ± 3
Porphyries (IG, CO/ME)	20 ± 5	Quartzites (EE, FI)	20 ± 3
Rhyolite (IG, ME)	25 ± 5	Sandstone (SE, ME)	17 ± 4
Schists (EE, ME)	12 ± 3	Shales (SE, VF)	6 ± 2
Siltstones (SE, FI)	7 ± 2	Slates (EE, VF)	7 ± 4
Sparitic limestones (SE, ME)	10 ± 2	Tuff (IG, FI)	13 ± 5

Appendix

Table 7: Qualitative indications to evaluate the damage factor of D

Disturbance factor D	D
Tunnel excavation by TBM or blasting of excellent quality (see <i>Figure 30 (a)</i>)	0
Tunnel excavation by hand of using a mechanical process rather than blasting, in poor quality rock. There are no squeezing problems leading to floor heave, or these are mitigated using a temporary invert (see <i>Figure 30 (b)</i>)	0
Tunnel excavation by hand of using a mechanical process rather than blasting, in poor quality rock. There are unmitigated squeezing problems leading to floor heave (see <i>Figure 30 (c)</i>)	0.5
Tunnel excavation using blasting of very poor quality, leading to severe local damage (see <i>Figure 30 (d)</i>)	0.8
Slope created using controlled, small scale blasting of good quality (see <i>Figure 30 (e)</i>)	0.7
Slope created using small scale blasting of poor quality (see <i>Figure 30 (f)</i>)	0.7
Slope in very large open pit mine, created using heavy production blasting (see <i>Figure 30 (g)</i>)	1
Slope in very large open pit mine, created using mechanical excavation in softer rocks (see <i>Figure 30 (h)</i>)	1

Appendix

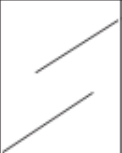
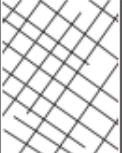
STRUCTURE		SURFACE CONDITIONS				
		VERY GOOD Very rough, fresh unweathered surfaces.	GOOD Rough, slightly weathered, iron stained surfaces.	FAIR Smooth, moderately weathered and altered surfaces.	POOR Slickensided, highly weathered surfaces with compact coatings or fillings with angular fragments.	VERY POOR Slickensided, highly weathered
	INTACT OR MASSIVE Intact rock specimens or massive in situ rock with few widely spaced discontinuities.	90			N/A	N/A
	BLOCKY Well interlocked undisturbed rock mass consisting of cubical blocks formed by three intersecting discontinuity sets.		70			
	VERY BLOCKY Interlocked, partially disturbed mass with multi-faceted angular blocks formed by 4 or more joint sets.			50		
	BLOCKY DISTURBED/SEAMY Folded with angular blocks formed by many intersecting discontinuity sets. Persistence of bedding planes or schistosity.				30	
	DISINTEGRATED Poorly interlocked, heavily broken rock mass with mixture of angular and rounded rock pieces.					20
	LAMINATED/SHEARED Lack of blockiness due to close spacing of weak schistosity or shear planes.	N/A	N/A			10

Figure 29: Representation of the GSI system according to Marinos et al. (2005)



Figure 30: Different construction cases related to the values of the disturbance factor D (proposed) (pictures (a)-(g) after I. Garcia Mendive and picture (h) after SRK consulting and Raimond Spekking, Via wekimedia Commons).